MECHANICAL PROPERTIES OF BULK NANOCRYSTALLINE AUSTENITIC STAINLESS STEELS PRODUCED BY EQUAL CHANNEL ANGULAR PRESSING

A Thesis

by

JEREMY ORION GONZALEZ

Submitted to the Office of Graduate Studies of
Texas A&M University
in partial fulfillment of the requirements for the degree of

MASTER OF SCIENCE

August 2011

Major Subject: Materials Science & Engineering

Mechanical Properties of Bulk Nanocyrstalline Austenitic Stainless Steels Produced by Equal Channel Angular Pressing

MECHANICAL PROPERTIES OF BULK NANOCRYSTALLINE AUSTENITIC STAINLESS STEELS PRODUCED BY EQUAL CHANNEL ANGULAR PRESSING

A Thesis

by

JEREMY ORION GONZALEZ

Submitted to the Office of Graduate Studies of
Texas A&M University
in partial fulfillment of the requirements for the degree of

MASTER OF SCIENCE

Approved by:

Chair of Committee,	Xinghang Zhang
Committee Members,	Karl T. Hartwig
	Lin Shao
Intercollegiate Faculty Chair,	Ibrahim Karaman

August 2011

Major Subject: Materials Science & Engineering

ABSTRACT

Mechanical Properties of Bulk Nanocrystalline Austenitic Stainless Steels Produced by Equal Channel Angular Pressing. (August 2011)

Jeremy Orion Gonzalez, B.S., Texas A&M University, Kingsville

Chair of Advisory Committee: Dr. Xinghang Zhang

Bulk nanocrystalline 304L and 316L austenitic stainless steels (SS) were produced by equal channel angular pressing(ECAP) at elevated temperature. The average grain size achieved in 316L and 304 L SS is ~ 100 nm, and grain refinement occurs more rapid in 316 L SS than that in 304L. Also, the structures are shown to retain a predominant austenite phase. Hardness increases by a factor of about 2.5 in both steels due largely to grain refinement and an introduction of a high density of dislocations. Tensile strength of nanocrystalline steels exceeds 1 GPa with good ductility in both systems. Mechanical properties of ECAPed 316L are also shown to have less dependence on strain rate than ECAPed 304L. ECAPed steels were shown to exhibit thermal stability up to 600^{o}C as indicated by retention of high hardness in annealed specimens. Furthermore, there is an increased tolerance to radiation-induced hardening in the nanocrystalline equiaxed materials subjected to 100 keV He ions at an average dose of 3-4 displacement-per-atom level at room temperature. The large volume fraction of high angle grain boundaries may be vital for enhanced radiation tolerance. These nanocrystalline SSs show promise for further research in radiation resistant structural materials for next-generation nuclear reactor systems.

DEDICATION

For my family, my beloved, and for those I've loved and those I've lost

ACKNOWLEDGEMENTS

I am indebted to my advisor Dr. Xinghang Zhang for making this work possible. I could not have reached this point without his patience, guidance, and encouragement. I would also like to express my gratitude to my committee members, Drs. Shao and Hartwig, not only for their enduring patience and helpful suggestions, but for providing and allowing the usage of their facilities. Cheng Sun, David C. Foley and Robert Barber were instrumental in helping with the design, execution, and understanding of ECAP experiments. Daniel Bufford, Yue Liu, and Byoungsoo Ham gave much of their time to help with microscopy for which I am very grateful.

TABLE OF CONTENTS

Page

LIST OF FIGURES

FIGURE Page

LIST OF TABLES

1. INTRODUCTION

The objective of this study is to refine the microstructure of bulk AISI 304L and 316L extra-low-carbon grade austenitic stainless steels (SSs) by an important severe plastic deformation (SPD) technique - equal channel angular pressing (ECAP). The microstructure, mechanical properties and thermal stability of the as-processed material are investigated. Preliminary ion-irradiation experiments were performed in order to gauge efficacy in resisting radiation-induced damage (such as radiation hardening). The introduction section focuses on radiation damage in steels and grain refinement via ECAP technique.

1.1. Austenitic Stainless Steels

Austenitic stainless steels represent both the greatest tonnage in world production and cover the widest spectrum of use. The class of so-called chromium-nickel austenitic SSs possesses nonmagnetic face-centered cubic (fcc) structure. Typical chromium-nickel compositions for the 304L and 316L steels are 18.0 – 20.0% Cr, 8.0 – 10.5% Ni and 16.0 – 18.0% Cr, 10.0 – 14.0% Ni respectively. As expected, the low-carbon grade SSs exhibit lower yield and ultimate tensile strengths, but this can easily be enhanced by cold-working, and especially SPD techniques such as ECAP. Stainless steels are attractive in industry primarily because of their corrosion resistance. As such, austenitic SSs find use in the chemical industry as a standard material of construction, in architecture and building construction, in surgical implants (particularly the 316L type), and, relevant to our interests, in the construction of nuclear power facilities.

This thesis follows the style of *Journal of Nuclear Materials.*

1.2. Radiation Damage and Tolerance in Metals

1.2.1. Microstructural Evolution

Nuclear transmutation of components within nuclear reactors yields production of He nuclei, which are also called alpha (α) particles or He ions at a very high rate. These products have long been recognized as a leading cause of detrimental effects in the material properties of reactor components which are in an environment constantly exposed to these transmutation products. It is, in fact, the main determining factor in component swelling and embrittlement. Fig. 1.1. shows a typical microstructure of neutron-irradiated 316L SS wherein a high density of irradiation-induced voids are observed.

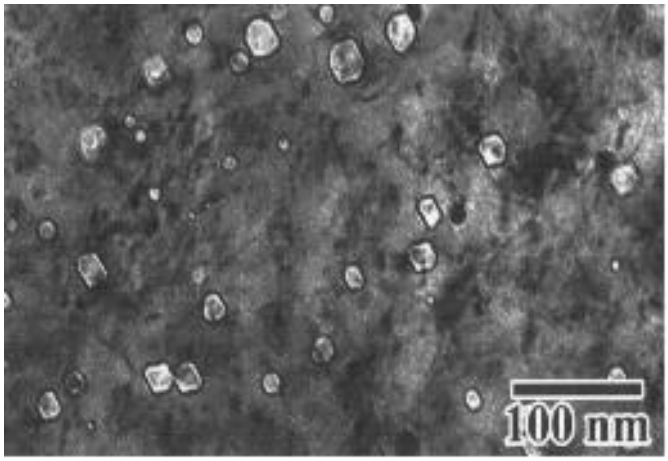

Fig. 1.1. - Microstructure of neutron-irradiated 316L stainless steel [1]

Atoms in a crystalline array or lattice are displaced from their usual sites by incident radiations. The types of radiations include uncharged particles such as photons and neutrons and charged particles such as electrons and ions (protons are essentially hydrogen ions, H^+). The simplest types of damage which may be produced are interstitial atoms and the

corresponding vacant lattice site. A single interstitial atom is formed when an atom is taken from the surface of a crystal and placed in one of the underlying interstices of the crystal lattice. Likewise, a vacancy is generated when an atom is taken from an interior lattice site and placed elsewhere within the crystal or even on the surface of the crystal. Both cases raise the overall energy of the lattice. Electrical neutrality is always maintained in the formation of these so-called point defects. At a given temperature, the equilibrium concentration of these point defects, C_v, depends on their energy of formation.

$$C_v \sim \exp\left[-\frac{E_f}{KT}\right] \tag{1}$$

Point defects are mobile. Rather than sit immobile in a lattice site (represented energetically as a well of potential energy), thermal vibrations increasing with rising temperatures increase the probability that a defect, like an interstitial atom, for example, will jump to an energetically identical adjacent interstitial site. Similarly, neighboring atoms to vacancy sites acquire an increasing probability to jump into the vacant site, in effect, causing the vacancy to "jump around" like an interstitial atom. Forces exist between like and unlike defects which lead to clustering, a phenomenon in which point defects coalesce to one another. In the ideal scenario, interstitial atoms and vacancies will attract one another and "cancel out", restoring the crystallinity of the lattice. The more typical scenario, however, is the grouping of defects. Pairs of interstitial atoms are called di-interstitials and pairs of vacancies are called di-vacancies. These are the simplest aggregates of point defects. The technological importance of these defects, however, is scarcely concerned with one- two- and three-point defects. Indeed, the technological interest focuses more on clusters that are many

times larger. Aggregates of these defects form one atom thick platelets which lie between adjacent close-packed planes in crystal lattices.

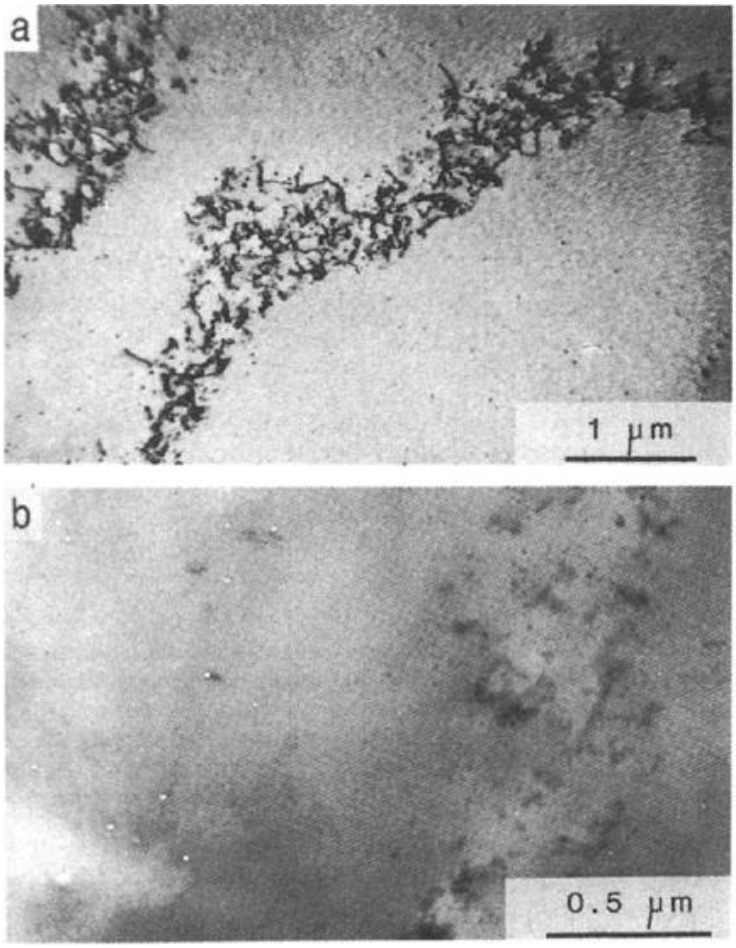

Fig 1.2. – TEM micrographs of dislocation networks and accumulated voids in neutron-irradiated in pure copper [2]

As reviewed by Mansur et al.. [3], there are critical quantities associated with swelling. These critical quantities arise as roots to the equation

$$\frac{dr_c}{dt} = \frac{\Omega}{r_c}[Z_v^c D_v C_v - Z_i^c D_i C_i - Z_v^c D_v C_v^e(r_c)] \quad (2)$$

Here the quantities are as follows: r_c denotes cavity radius, t time, and Ω the atomic volume. The symbol Z^c denotes capture efficiency of a cavity for point defects and D is the point defect diffusion coefficient. The total point defect concentrations are denoted by C which depend on irradiation variables and materials properties such as dose rate, temperature, microstructual sink densities and point defect properties [3]. He has a low solubility in metals [4-5], and so interstitial He atoms introduced in to a metal matrix either by transmutation or high energy bombardment (implantation) can rapidly precipitate out at nearby sinks such as vacancies and grain boundaries. A common parameter for describing radiation damage is the so-called displacement per atom (DPA). It is a measure of the average displacements of lattice-site atoms due to collision with oncoming particles and with collisions between displaced atoms with other lattice-bound atoms. But lattice-site atoms may also be ejected as He-atom clusters grow. It has previously been estimated that these cavities yield bubbles at pressures of several GPa. Furthermore the cavities formed during accumulation of He, which results in void swelling, is stable in a broad temperature range of 350 to 700^{o}C [4]]. These effects are more than a microscopic and seemingly trivial phenomenon. This is not so, as physical changes to the dimensions at the macroscopic level also occur. These macroscopic changes are termed dimensional instabilities and include swelling, shrinking, creep, and growth. Several of these may occur together. As previously discussed, swelling can occur by the formation of cavities generated by implantation of He or displacement of lattice-site atoms. Shrinkage happens when the material forms more dense phases (there is no material loss). Primary knock-on atoms (pka) impart to the collision site so much energy that it creates a cascade of damage events. It's understood that these microstructural changes relate to the

mechanical property changes in austentitic SS. The specifics of the damage microstructure depend on the type of stainless steel and the types of defects which evolve. There are Frank loops which are clusters of faulted, interstitial-type dislocation loops. Once nucleated, they continue to grow as they have a tendency to absorb other self-interstitials. There are perfect dislocation loops which can glide and continue to expand also by absorption of self-insterstitials. Networks of dislocations and large loops can climb and glide until they annihilate with neighboring dislocation segments of opposite types. These microstructural evolutions are accompanied by changes in mechanical properties. In general, yield stress tends to increase (irradiation hardening). For annealed steels, the yield stress increases with dose up to a peak value and steadily decreases suggesting that there is no apparent steady state. Trends for cold-worked material indicate that yield stress follows a similar trend, albeit in a less pronounced way. Changes in strength, ductility, and fracture toughness are strongly related to the evolution of the damage microstructure. The mechanism by which the microstructure changes depends on temperature. Low temperature microstructures are dominated by dislocation loops and network dislocations. At intermediate and high temperatures, voids and precipitates become more important [6]. This leads to the current problem, including void swelling and radiation embrittlement. In order to be considered for use in construction, a material must exhibit a degree of superior radiation damage tolerance. A radiation damage tolerant material must be able to absorb high energy particle radiation induced defects while delaying the onset of the void swelling and alleviate radiation embrittlement. Embrittlement of material shortens the operation life of the material and endangers personnel and environment. When exposed to proton and neutron radiation, austenitic SSs are observed to retain much of their strain-hardening capabilities. The

hardening capabilities result from such characteristic deformation mechanisms of austenitic stainless steels: dislocation slip and mechanical twinning. As expected, both mechanisms are usually restricted to the {111} slip planes. Irradiation by alpha particles has been observed to increase the tendency of twinning during plastic deformation such that the microstructure changes from one mode of defects to another as a function of increasing dose [7]. Twins are formed due to glide of Shockley partial dislocations. Since twinning can produce a high shear strain within twin bands, a significant strain can be observed at the macroscopic level when twinning occurs with irradiation on multiple slip systems (such as is the case with FCC materials). Eventual suppression of cross-slip further confines dislocation pile-ups to these slip planes and thus increases the strain-hardening rate. Twinning will create internal barriers to slip phenomena which break down grains in to smaller grains [8].

1.2.2. Radiation Hardening

1.2.2.1. General Hardening Mechanisms

Much of what was originally understood about the effects of radiation damage was due to studies on pure metals during the mid 20th century. The discovery of radiation-induced void swelling in solids along with a renewed interest in next-generation nuclear power generating systems shifted the focus from fundamental studies to practical and realistic alloys. Nevertheless, any sufficient survey of the mechanisms by which microstructures produce macroscopic changes in mechanical properties such as hardness should include what is already known and thoroughly studied in pure metals. Still, a great effort has been made to explain radiation hardening in metals and to correlate change in strength with the number density and size of radiation-induced defects and with irradiation dose. Radiation of FCC and

BCC metals causes an increase in the yield stress, σ_{YS}, by two mechanisms: source hardening and friction hardening. Source hardening is defined by the increase in stress required to start a dislocation moving along its glide plane. Friction hardening is due to obstacles, natural and radiation-induced, that occur along the glide plane which restrict the ease by which mobile dislocations can move. When an FCC metal has been irradiated, defect clusters can be induced near Frank-Read sources. When this happens, the stress required to expand the loops and to permit source multiplication increases. Friction hardening arises from a combination of short-range and long-range stresses due to obstacles that dislocations may encounter such as dislocation networks and defect clusters, loops, precipitates, voids, etc. These long-range stresses occur because of interactions of the stress field of one dislocation with that of another while short-range stresses result from the interaction of mobile dislocations with discrete obstacles present on current glide planes and arise only when the dislocation actually contacts the obstacle. When these obstacles are distributed over a glide plane, the friction stress depends largely on the average separation between the various obstacles. A strong obstacle, such as a precipitate, will block the motion of a dislocation, but not entirely. A large enough stress will cause the blocked dislocation to bow out between any two adjacent obstacles the dislocation line happens to contact during its movement. When any two segments of this dislocation line contact, they will annihilate and the dislocation segments will “pinch off”, allowing the remainder of the line to glide continuously along the plane until it encounters another obstacle. The pinched off segments form a dislocation loop around the obstacle, becoming an even stronger obstacle for future dislocations that may encounter these obstacles. The interaction between dislocation lines

and voids is similar except that there is no resulting dislocation loop around the void(s) according to Fundamentals of Radiation Materials Science: Metals and Alloys.

Multiple hypotheses have been proposed to explain just how these factors add up in the overall scheme, but the best studied variable is the increase in yield stress, $\Delta\sigma_{YS}$, as a function of dose. The simplest model for hardening as a function of dose is in the form of a power law expression [9]:

$$\Delta\sigma_{YS}=h\varphi^{n} \tag{3}$$

where φ is the radiation fluence which can be replaced by equivalent parameters such as DPA. The exponent is found for different systems by varying dose (again, only pure metals have been considered in the literature). However, as dose increases, a saturation point is reached and this model can no longer be considered valid. A two-parameter equation is then suggested for higher doses. As proposed by Makin and Minter, the power law expression can be modified for the saturation region:

$$\Delta\sigma_{YS}=A[1-\exp(-B\varphi)]^{1/2} \tag{4}$$

Here, A and B are parameters which depend on the nature of the obstacles as they are related to the activation energy for overcoming obstacles. This model is mostly empirical.

1.2.2.2. FKH Hardening Model

Helium bubbles distributed throughout the material matrix also lead to hardening phenomena. The dominant parameter is the density of helium bubbles within the material in any region (usually observed by TEM). The magnitude of the He bubble hardening can be estimated by treating the bubbles as weak obstacles using a hardening relationship proposed by Friedel-Kroupa-Hirsch (FKH).

$$\Delta\sigma = \frac{1}{8} M\mu b d N^{\frac{2}{3}} \tag{5}$$

where M is the Taylor factor, 3.06 for equiaxed FCC metals, μ is the shear modulus, b is the Burgers vector, N is the bubble density.

1.2.2.3. Dispersed Barrier Model

The increase in yield stress can be estimated by considering the increase in applied stress required to move a dislocation through a field of obstacles.

$$\Delta\sigma_y = M\mu\alpha b\sqrt{Nd} \tag{6}$$

where α is the barrier strength, N is the average loop density and d the average loop diameter. The typical barrier strength of dislocation loops can be taken as 0.45 [10]. Defect cluster density and cluster loop diameter have been shown to increase with increasing dose in neutron-irradiated material [11].

1.2.2.4. Helium Interstitials

Embedded helium ions may act as interstitials either as individual atoms or as clusters. It is shown by atomic simulations that He interstitials near a dislocation can migrate

towards the dislocation core and thus resist the glide of dislocations at low temperature. A high concentration of He interstitials leads to hardening especially when approaching the critical value of ~1 atomic percent. [12] , The effect of cascade induced gas resolution on bubble formation in metals [10].

1.3. ECAP

It is recognized that plastic deformation is an effective method of microstructural refinement and mechanical properties improvement. Some of the oldest metal-forming operations, such as extrusion, forging, and rolling were traditionally used to accomplish this goal. Traditional though they may be, these techniques comprise certain limitations. The billets will undergo significant reduction in initial cross section dimensions as a result of the mechanisms invoked in each of these processes and, consequently, lead to a strong stress-strain non-uniformity of the material. To facilitate these processes, powerful machines and expensive tools are often required. ECAP was first proposed by Dr. Vladimir M. Segal. He noted that simple shearing produces a “near ideal” deformation for materials. In the beginning, the methods for achieving this deformation were only applicable to relatively small volumes and so remained impractical on a large, manufacturing scale [4,5]. He solved this problem by designing a special plastic deformation method which he called equal channel angular extrusion (ECAE). The tool's design is a block with two intersecting channels of identical cross-sections. Though a variety of tool angles are plausible in theory, it's been suggested that a tool angle of 90^{o} is the most practical and most effective. A well-lubricated billet of slightly smaller cross section is inserted in to one of the channels and a punch extrudes it through in to the second channel by which it exits. The billet moves as a

rigid body and deformation is achieved where the two channels intersect, which is called the shear plane. A rough schematic diagram is shown in Fig. 1.1.

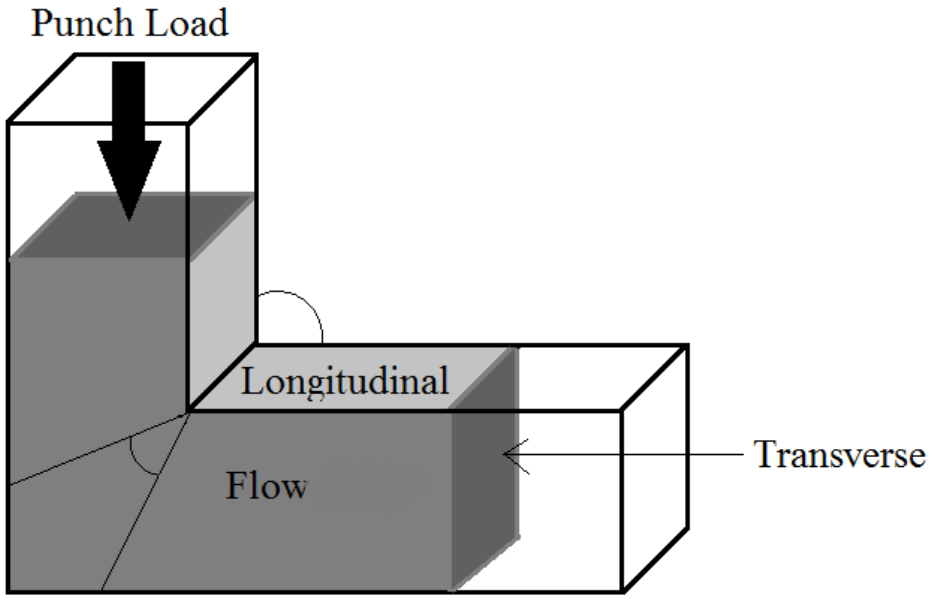

Fig. 1.3. - Schematic of ECAP

Though all the tooling and engineering are complex, the mechanism is simple. All the deformation takes place in thin layers at the shear plane so that the entire billet (except the end regions) is deformed in roughly the same uniform manner. Figure 1.4 shows how an engraved grid can be used to demonstrate the uniform deformation of volume elements. This Figure also shows how this uniform deformation does not apply to the end regions. All the volume elements represented by the grid are deformed to the same dimensions in the same direction.

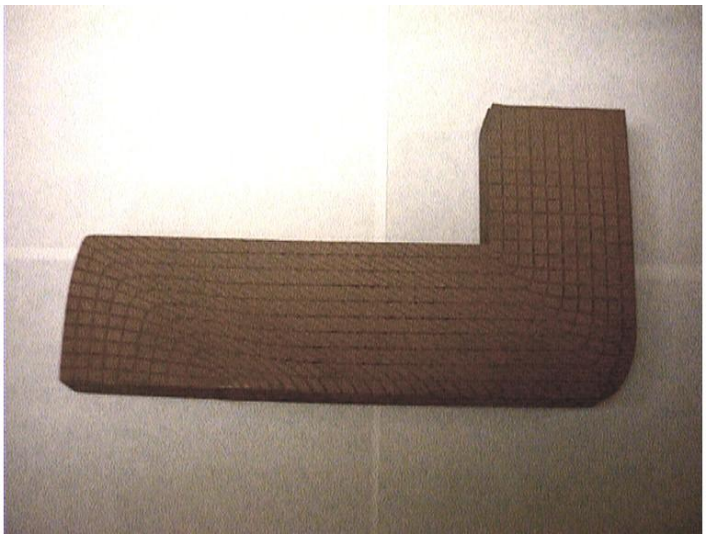

Fig. 1.4. - Partially-extruded copper billet with grid lines to show uniform distortion of material elements

Since shear strain is uniform throughout the sections of the billet which pass through the shear plane, it is possible to determine the distortion of volume elements at any point. Dr. Segal noted that the theoretical prediction and the actual distortion of a grid on a specimen are indistinguishable. Punch pressure, p, and increment of strain intensity, $\Delta\epsilon_i$, are functions of the angle 2φ between the channels and the material's flow stress, Y.

$$\frac{p}{Y} = \Delta\varepsilon_i = \frac{2}{\sqrt{3}}\cot an\varphi \tag{7}$$

Calculations of reduction ratio, RR, and area reduction, AR, for equivalent "ideal" forming operations accomplished by change of billet cross-section area from F_0 to F confirms that, indeed, a large and uniform strain intensity per pass without much reduction in cross-section dimensions can be achieved in material processed by ECAP.

$$RR = \frac{F}{F_0} = \exp(\Delta\varepsilon_i) \tag{8}$$

$$AR = (1 - RR^{-1})100\% \tag{9}$$

ECAP's appeal stems from the possibility that multiple extrusions with large deformations can be performed on the same billet. Indeed, the total strain intensity as a function of total number of extrusions, ε_n, scales proportionally to the number, N, of passes.

$$\epsilon_n = N\Delta\epsilon_i \tag{10}$$

This can be easily extended to an equivalent reduction ratio

$$RR = \exp(N\Delta\varepsilon_i) \tag{11}$$

The structural effects imparted by ECAP depend largely on the so-called route. Since the initial billet cross-section is preserved, it can be re-inserted in to the channel and further extruded in the exact same manner. Another aspect of the tooling is that the channel cross section is usually something symmetric like a square or circle. To that end, some combination of successive $(\frac{360}{n})^{\circ}$ rotations (depending on rotational symmetry of the cross section shape) of the punch face about the longitudinal axis of the extruded billet (the punch face is literally that face which is in contact with the punch during the extrusion) can be performed in between successive passes. The type of rotation between extrusions is called the route. To understand this relation between punch face and rotation, one can simply consult Fig. 1.3.

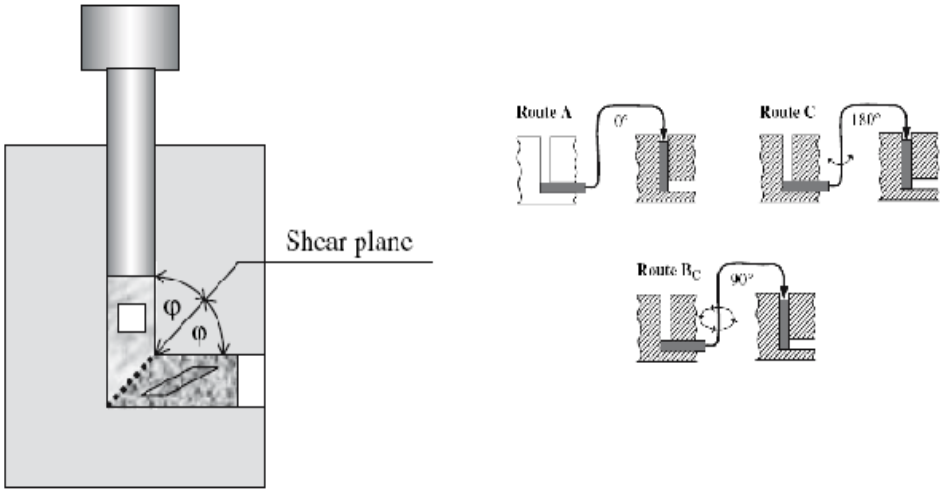

Fig. 1.5. - Schematic of the ECAP process and possible routes

In his original paper, Segal noted two extreme cases of routes. Route A is the simplest in which the billet's orientation is the same after each pass (Fig. 1.5). In this route, material elements are further distorted in the same manner with each successive pass and as a result, laminar structures are produced with heavy texture along the flow direction (FD) [13],[14]. Where interest in producing fine grain structures, a single route A pressing would be insufficient[15],[16] The other extreme case is route C in which the billet is rotated 180^{o} between passes. Material elements are uniformly deformed after an even-number of passes and culminates in an equiaxed grain structure [13].

Since then, other routes have been studied and identified. Of particular interest, especially for this study, is the so-called B route. Route B is accomplished by a 90^{o} rotation between passes. A further distinction from the previous routes is that route B's efficacy is also affected by the direction of successive rotations. This is evident after the second pass in which the user has the option to either rotate the billet a further 90^{o} in the same direction

between passes (e.g.successive clockwise rotations between passes) or, to rotate it 90^{o} back-and-forth between the original and the second orientation (e.g. alternating between clock-wise and counter-clockwise between passes starting with the first). The former is called route Bc while the latter is B_A. [16] summarizes how material elements are distorted by any of the mentioned routes. After about four passes, many materials show signs that the grain structure is approaching that of equiaxed grains since subgrain boundaries evolve rapidly into high angle grain boundaries. It has been proposed that route Bc has the greatest potential for producing a homogeneous ultrafine-grained microstructure [17].

1.4. ECAP and Radiation Damage Tolerance

A material's ability to resist radiation damage lies largely on how well its microstructure can permit the removal of vacancies of interstitials in roughly equal numbers. Radiation-induced swelling is due largely to a phenomenon of incomplete interstitial-vacancy recombination. As stated earlier, incoming particle radiation displaces atoms from their usual lattice sites. As such, vacancies are formed at former lattice sites while displaced atoms become interstitials. Within the material there are so-called preferential sinks for interstitials. Interstitials tend to migrate towards these sinks leaving vacancies behind. As a result, vacancies cannot recombine with interstitials and thus vacancies tend to cluster together by Ostwald ripening until they grow large enough to become voids. Large voids ultimately culminate in volume swelling of material. A low-enough concentration of dislocations actually act as preferential sinks for interstitial, and hence leaving vacancies behind. However, if dislocation density is high enough, then, even vacancies may migrate towards dislocations. A similar occurrence happens in fine-grained materials, with grain boundaries

acting as a kind of defect trapping site. It is speculated that grain boundaries act as a defect sink similar to other such interfaces. It has been demonstrated time and again that material with a high fraction of grain boundaries, such as ultra-fine grain and nanocrystalline Cu, Au, and Ni, have improved resistance to irradiation resistance. However, it is only speculated just what kind of interaction takes place and how it acts to trap defects. Typically, the temperatures in many irradiation experiments are too low to permit sufficient mobility of defects. Yet, there is a definite interaction, regardless of temperature, between point-defects and a higher fraction of grain boundaries. Elucidation of involved mechanisms is further complicated by the fact that radiation damage extends from an atomic to a macroscopic time and length scale. Furthermore, critical processes involving individual point-defect migration are difficult to observe experimentally and simulations are really only possible for picoseconds to nanosecond time scales. However, Bai et al.. have used a combination of modeling and simulation techniques on Cu (the standard and best understood FCC system) to better understand the role of grain boundaries on the behaviors of defects on a picoseconds to microsecond time scale. Their results suggest that grain boundaries have a “surprising loading-unloading” effect. At a small enough grain size and upon irradiation, interstitials are loaded in to the grain boundary and then act as a source which emits interstitials back in to the grains which annihilate any vacancies which happen to be present within the grain. This effect has a much lower energy barrier than conventional defect migration and so is also effective in annihilating immobile vacancies in the bulk. This, they conclude, gives fine or nanocrystalline grained material a kind of self-healing property to irradiation damage [18]. This effect can be illustrated by Fig. 1.6.

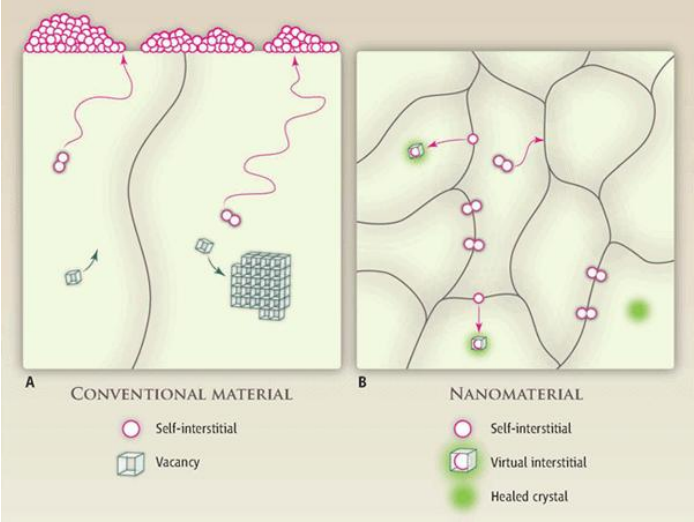

Fig. 1.6. - (A) A conventional (coarse grained) material. Interstitials aggregate at the surface causing swelling.. (B) A nanocrystalline material exhibiting the "self-healing" mechanism

At this point, the utility of ECAP in this project can now be stated. Material subjected to the intense plastic strain of the material produces fully-dense microstructures with ultrafine grain sizes in the submicrometer or nanometer range. The production of nanocrystalline grains has been demonstrated time and time again by ECAP [19], [20], [21], [22], [23],[24], [25], [26], [27], [28], [29]. The size and shape of these refined grains varies as a function of both the number of extrusions (passes) and the rotation of the billet between subsequent passes. As a rule, a higher number of passes leads to further reduction in grain dimensions as well as eventual equiaxing of grains. Apart from the grain size reduction, there is also the inevitable increase in dislocation density one would expect from such severe plastic deformation. As such, ECAP promises to fulfill at least two criteria for inhibiting void swelling in materials by reducing the grain size of bulk materials as well as leading to a high density of dislocations for defect trapping.

1.5. Size Dependent Radiation Damage in Multilayers

It has been proposed that metallic multilayers may aid in the mitigation of irradiation-induced defects using the rationale that the interfaces between layers may act as sinks for point-defects and embedded particles while enhanced diffusivity near the interface leads to more frequent recombination and annihilation of other point defects. This has been demonstrated in a Cu/Nb 4nm layer system, albeit for a low energy of 33 keV. Nevertheless, the exhibited effects of blistering and mechanical degradation evident in bulk single phase Nb and Cu and "large" layer sizes of 40 nm under the same conditions were not evident for this and for similar fine structures such as in Cu/V, Al/Nb and Fe/W multilayers [30],[31]. Thus, there is a relationship between layer thickness and resistance to irradiation-induced effects as shown in Fig.1.7. Indeed, Li et al.. have shown that finer layer thickness in Fe/W system resists radiation hardening (Fig. 1.8.).

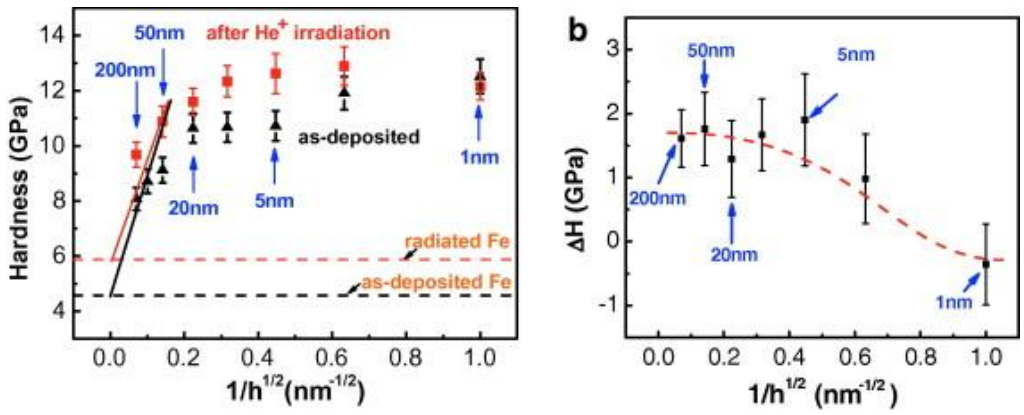

Fig. 1.7. - plots showing hardness and hardness change as functions of layer thickness ($1/h^{1/2}$)

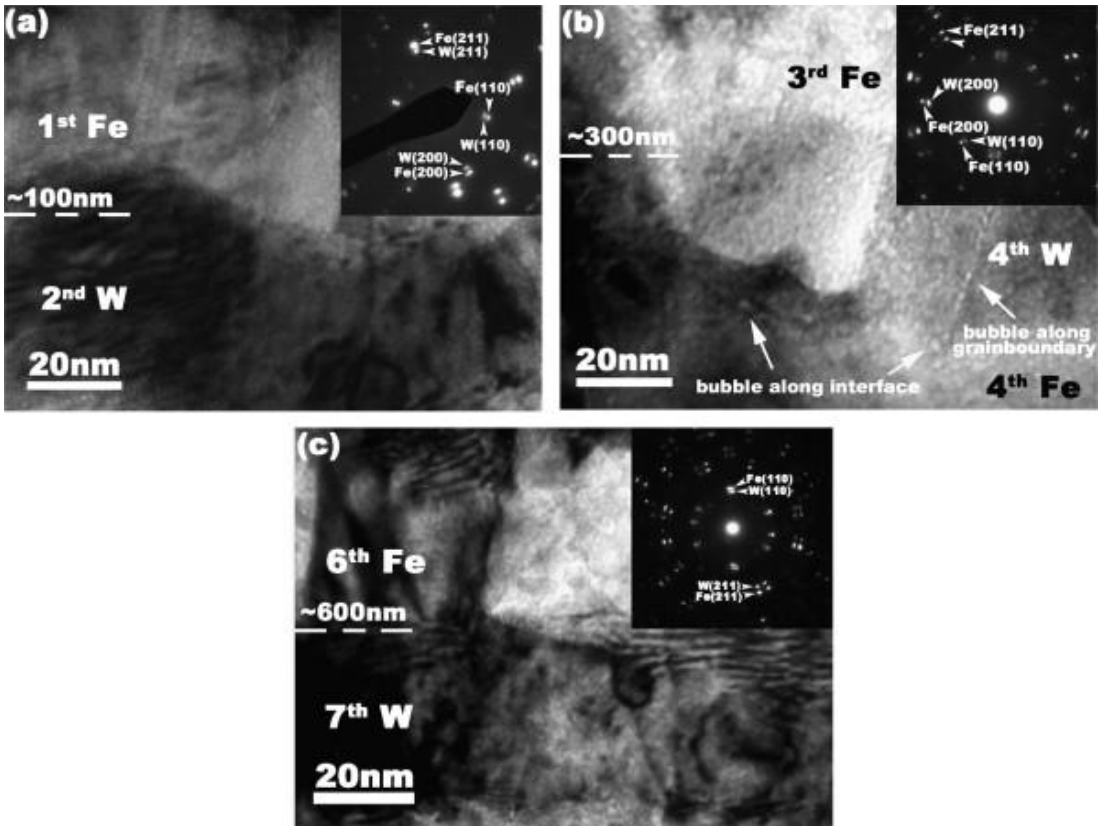

Fig 1.8. - TEM micrographs showing how successive views deeper below and beyond the radiation damage region remains stable and intact after He ion irradiation

A finer layer thickness increases the ease by which point defects can diffuse to interfaces in much the same way as fine (nanocrystalline) grains. Even a thin sheet of Cu responds to irradiation in the same way as bulk material [31]. These systems are chosen based on their inherent immiscibility. Intermixing may destroy interfaces which are the key component in the mitigation of irradiation damage. While immiscibility is a key parameter, there are further parameters within any applicable system which may be varied or control. Such microstructural features as coherent and incoherent interfaces may be tailored since the behavior of irradiation defects differs for each. Indeed, Zhang et al.. have noted that the

interface between Cu and Nb layers may be very effective in storing irradiation defects, pending a more thorough understanding of the crucial parameters such as critical thickness and dose [30],[31]. The previously-mentioned theoretical treatment of Bai et al.. implies that such a generalized mechanism can also apply to interfaces between immiscible materials wherein a nanostructure will be preserved [32].

2. EXPERIMENTAL METHODS

Material subjected to ECAP, thermal treatment or irradiation damage undergoes a variety of microstructural changes. These changes may be in the grain size and morphology but can also result in phase transformations. These material changes can be tracked and characterized via a variety of different analytical techniques. Experimental techniques and rationale are discussed in this section.

2.1. Materials

Commercial 304L and 316L stainless steel were used in this study. The starting material for each is a long bar (rod) of pre-extruded material of an approximately one inch square cross section from which the billets were cut. The cross-section of specimens was reduced accordingly by milling in order to accommodate for thermal expansion of material. A nominal composition for each is given in Table 2.1.

Table 2.1. Nominal composition

Wt. %	304L	316L
Cr	18.19	15.94
Ni	8.04	10.13
Mn	1.68	1.38
S	0.03	0.03
Si	0.3	0.47
N	0.08	0.77
P	0.026	0.028
Mo	0.12	2.01
C	0.02	0.028
Fe	Balance	Balance

2.2. Processing

There were different processing conditions for different specimens. Table 2.2 contains the key details and identifiers that will be referenced throughout this thesis.

Table 2.2. Processing parameters and identifiers

Specimen	**Billet Dimensions**	**Route**	**Extrusion Temperature (^{o}C)**	**Identifier**
304L	.97" × .97" × 6"	2B	300	2B 300
	.725" × .725" × 6"	4Bc	500	4Bc 500
	.725" × .725" × 6"	6Bc	500	6Bc 500
316L	.97" × .97" × 6"	2B	300	2B 300
	.725" × .725" × 6"	4Bc	500	4Bc 500

All billets were furnace annealed for up to one hour at 1150 ^{o}C and subsequently quenched in air prior to extrusion. ECAP was carried out in a sliding wall die designed by Mr. Robert Barber and Dr. K. T. Hartwig. This was done by an MTS-controlled 225 ton (250 short ton) hydraulic press. For all extrusions, temperature was controlled by maintaining the die at the desired temperature so that extrusions could be carried out isothermally. Extrusion speed varied as a function of specimen, and pass number. The billets are then placed within the pre-heated die for approximately 30 min in order to reach extrusion temperature. Immediately after extrusion, the billet is removed quickly from the channel and quenched it in water. Maximum press load and die temperature were recorded during the extrusions and the dimensions of the extruded billet were recorded after cooling. This process was repeated for each extrusion.

2.3. Microhardness

Samples for hardness tests were prepared as follows: small plates were cut from the extruded 304L 2B300 and 316L 2B300 billets via electron discharge machining (EDM) and were further sectioned with a Buehler Isomet 1000 diamond wafer saw. The result was a small, rectangular plate that was then mounted in an acrylic mold with the surface of the specimen to be tested exposed on one end. Standard metallographic specimen surface preparation then followed with rough grinding with 400, 600, 800 and finally 1200 grit Silicon Carbide (SiC) grinding, followed by rough polishing with a 1 μm particle size alumina slurry and finally a 20 nm colloidal silica slurry final polishing. The sample is then fixed to a mount that will level the surface parallel to the sample stage on the indenter. It was later discovered with the 4Bc 500 and 6Bc 500 specimens that samples could be prepared much faster and with greater ease if done manually instead of mounted in the acrylic mold. Grinding and polishing was the same in both cases.

Hardness and elastic modulus of specimens were measured by using a Fischerscope HM 2000XYp micro/nanoindentor. The device is fully automatic and computer-controlled. The instrument is designed to measure Martens Hardness (according to ISO 14577) of materials. Meanwhile its operating software contains algorithms that allow the determination of indentation hardness, Vickers hardness, and the elastic modulus. The indenter is a 4-sided diamond pyramid (Vickers indentor tip) with a 136^{o} face angle. The indenter is lowered gradually on to the sample to avoid impact of sample surface. Test loads can range from 0.4 mN to 2000 mN. A load of 2000 mN was used in this study. The hardness measurement range is several to ~ 100 GPa. The sample is placed on the sample stage which is positioned under a microscope that has a digital camera that can be viewed on the computer screen. The

points for testing hardness are selected on an XY programming interface and then the experiment runs automatically. The plot of load versus depth (from a few nm to tens of microns) can be captured in real time on the computer screen. Once the measurements are done, the user can export the data (in our case, a Microsoft Excel Spreadsheet file) for analysis and report. The positions (x,y) on the sample to be tested can be programmed using a XY Programming feature available on the software. These points are accurate within ± 3 μm. 12 points were selected for each hardness measurement. The time for each indentation experiment was ~ 30 seconds.

2.4. Transmission Electron Microscopy (TEM)

Rods of 3 mm diameter were cut from the extruded billets via EDM to be used for TEM samples. Discs are cut from the rod using the same Buehler wafer saw. The disc was then mounted on to a small pyrex glass cylinder using crystal bond (an adhesive) which was then mounted in to a Gatan disc grounder to achieve parallel surfaces during the sample thinning process. The grinding and polishing are similar as for the microhardness samples. The specimen is ground and polished on one side to a 1 μm alumina final polish. Then the disc is flipped over and ground only up to a 600 grit grinding until the sample became approximately 80 μm thick. For our earlier series of TEM studies, the thinned disc (still mounted on the glass cylinder) was taken to a Gatan Dimpler where it was further thinned to approximately 20 – 30 μm using 10 μm diamond paste on a copper wheel. A final polish with 1 μm diamond paste on a cloth wheel followed. Constant attention was given in the dimpling stage as too much grinding would create a small hole that would invariably ruin the specimen for analysis. The last stage in the TEM sample preparation for this series required

that the sample be carefully removed from the glass cylinder. This was done first by heating the cylinder to about 170 ^{o}C to soften the crystal bond and then the disc was placed in a small portion of acetone to further dissolve any residual adhesive. A quick methanol wash removed any residue from the acetone wash. The disc is then inserted in to a Gatan 691 Precision Ion Polishing System (PIPS) in a mount designed to accommodate polishing of the specimen top and bottom. This was to ensure that none of the sputtered material would redeposit on the specimen thus compromising sample integrity. Each specimen prepared in this manner would require ~ 4 hours in the PIPS, using 3.5 keV Ar ions at an incident angle of 5 degrees with respect to the sample surface (top and bottom). The sample is regularly monitored via a built-in microscope and, by utilizing an internal light source, it can be determined when the sample is sufficiently thin by discerning a small hole that forms in the center of the sample. Once it has been decided that the sample is ready, it is then polished with 2-2.5 keV energy for 15 to 20 minutes to remove any potentially redeposited material. The sample is removed and ready for TEM.

More recently it was decided that this particular method was too cumbersome and lengthy for our purposes and so a quicker method was devised for the last set of TEM samples. As before, the disc is thinned on the Gatan 625 disc grinder to about a 100 μm thickness using 600 grit grinding. Afterwards, the disc is placed in a twin-jet electro polisher and sufficiently thinned by way of electrochemical polishing using a 10% (v/v) perchloric acid in ethanol solution and a 20 V potential. The polishing unit contains an infrared photosensor whose sensitivity could be varied so that once a small hole is formed, the polishing jets and electrochemical cell are switched off. The samples created in this way had the photosensitivity set to the most sensitive setting. The sample is then taken out and

immediately immersed in a 1 L beaker of distilled water to remove any residual solution. The procedure is repeated by using another beaker of distilled water to further dilute any residue. Finally, the sample is placed under a stream of distilled water for a final rinsing. This method produced excellent quality TEM specimens with a larger viewing area and in a fraction of the time that was required for the previously described method.

TEM experimetns were performed on a JEOL 2010 high resolution analytical transmission electron microscope operated at 200 kV with a point-to-point resolution of ~ 0.2 nm. Whenever selected area diffraction (SAD) is used, the aperture is large enough to represent the area under investigation. The images are captured digitally using software that is interfaced with the microscope.

2.5. X-Ray Diffraction (XRD)

This study uses a short-arm Bruker-AXS D8 X-ray Diffractometer. XRD Specimens were the same used for microhardness studies. Samples mounted in the acrylic mold are easily inserted in to the specimen holder. The free-standing (i.e. 4Bc 500 and 6Bc 500) specimens were fixed to the sample holder using clay. The scan rate was typically 0.01 degree/s and the range of 2θ varies from 30 to 90 degrees. Peak-matching was accomplished with the aid of a database supplied in the Bruker software.

2.6. Thermal Stability

In order to assess the stability of the processed microstructure, several annealing experiments were performed on sections taken from the extruded billets. A small plate from each billet was numbered by an electronic engraver and placed, in separate batches

depending on annealing temperature, in to a vacuum furnace and annealed at 400, 600, 700, and 800 ^{o}C for one hour and subsequently air-quenched. The samples were then ground and polished via conventional methods and their hardnesses as a function of annealing temperature were noted

Additionally, to assess grain growth or recrystallization temperature, as well as any possible phase transformations in the annealing region, small samples from the as-processed material were prepared for Differential Scanning Calorimetry (DSC) studies. Three 3 mm discs were mounted on a glass cylinder and ground until the mass of each was approximately 10 mg. To wit, three sets of DSC experiments were carried out for material processed at each condition. The heating rates are varied at 20, 40, and 80 ^{o}C/min, and the maximum temperature fixed at 720 ^{o}C.

2.7. He Ion Radiation

Two sets of He ion radiation were performed. The first was performed here at Texas A&M University (TAMU). The other at Los Alamos National Laboratory (LANL). In both cases, samples cut from the as-processed billets were prepared in a similar fashion to the microhardness specimens. In addition, the samples were polished using a vibration polisher to a 20 nm colloidal silica finish. This was done to minimize the surface roughness which would impede accurate measurements of post-radiation properties. The samples are placed on a sample holder. The samples were radiated with 100 keV He ions at 6×10^{16} ions/cm^2 at room temperature.

3. MICROSTRUCTURE AND MECHANICAL PROPERTIES EVOLUTION

3.1. Microstructure

3.1.1. X-Ray Diffraction (XRD)

XRD was performed to examine the microstructure of processed specimens. Determination of γ-austenite and α'-martensite peaks were based on d spacing calculations, using γ iron as a reference for austenite and α iron as a reference for martensite, and a comparison with literature. Spectra for the as-received and as-processed 304L stainless steel (SS) normal to the transverse direction of the processed billet are shown in Fig. 3.1. The fully-annealed as-received (AR) specimen indicates a predominantly γ-austenite phase. Subsequent processing at elevated temperatures (300^{o}C or greater) seems also to preserve the predominant γ-austenite with generation of a few stress-induced α'-martensite phases. The story is significantly different for 304L SS processed at room-temperature. The spectrum shows that α'-martensite dominates when processed at room temperature. This may explain the difficulty in achieving more than one extrusion at this condition as significant hardening occurs as shown later.

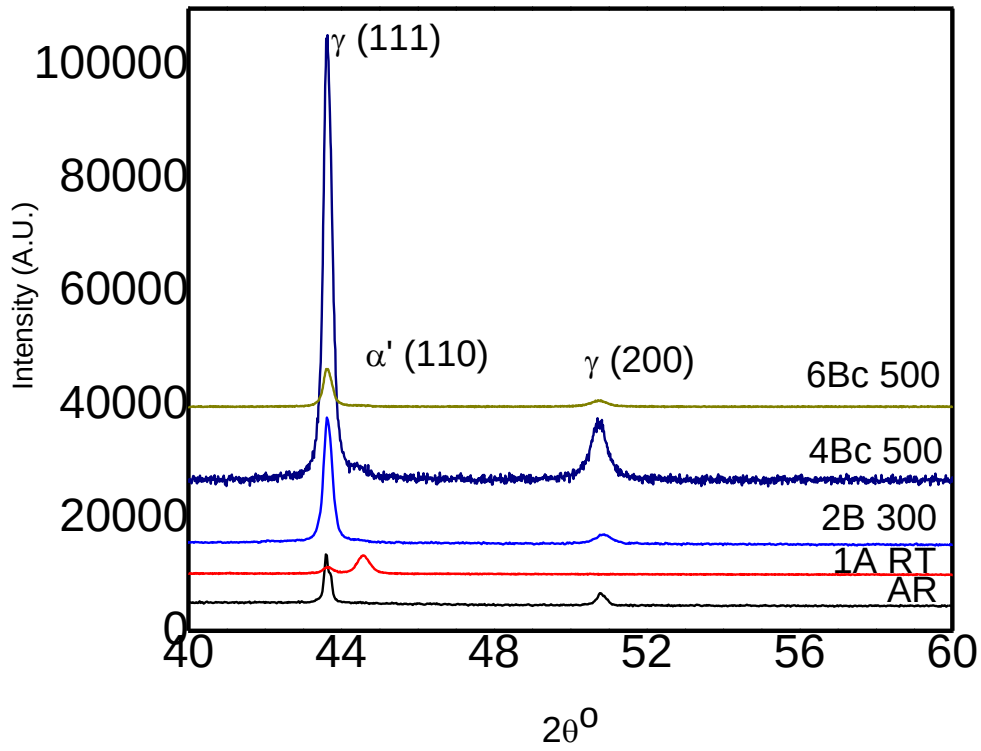

Fig. 3.1. – 304L XRD spectra for as-received and as-processed material

A similar situation arises in the 316L SS as shown in Fig. 3.2. Of worthy note is the fact that stress-induced martensite seems to be significantly suppressed. As shown by the 1A RT spectrum, unlike 304L 1A RT, a predominant γ-austenite is still preserved after room-temperature processing. Indeed, α'-martensite formation is still suppressed even after higher-temperature (300°C or greater) extrusions, and so does not appear in any significant quantity.

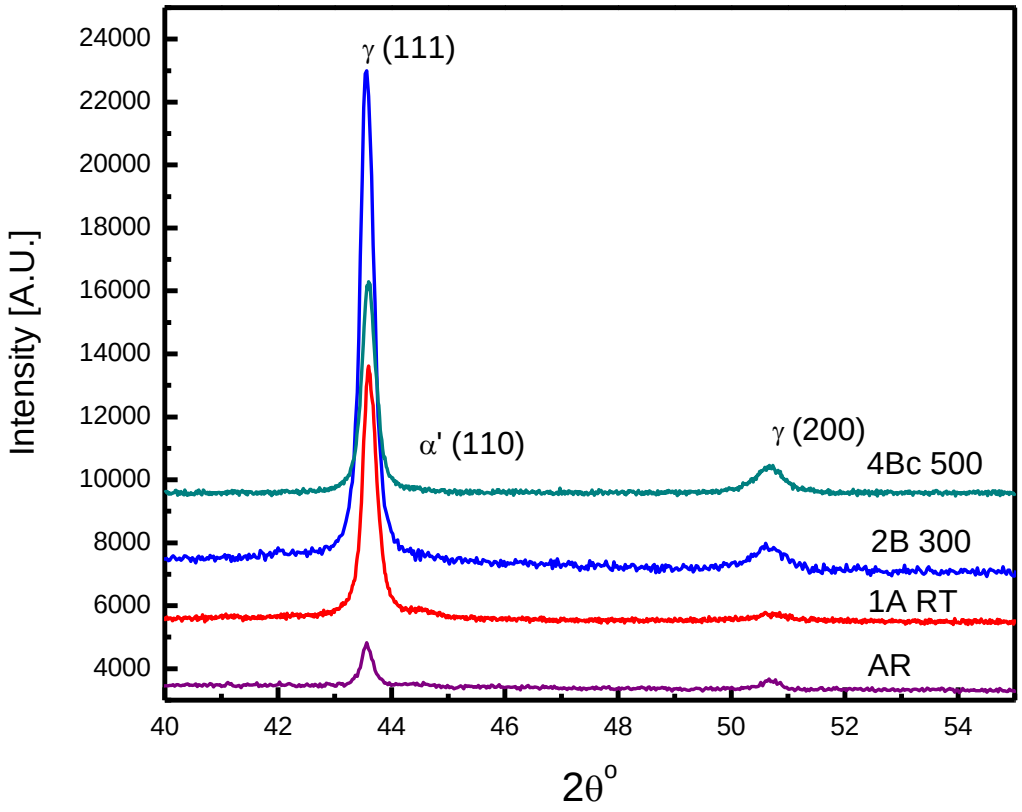

Fig. 3.2. – 316L XRD spectra for as-received and as-processed material

3.1.2. Transmission Electron Microscopy (TEM)

Bright-field plane-view TEM micrographs of representative areas were taken from the transverse and flow planes of the as-processed billets. The transverse view is discussed first. The transverse view in all cases shows a mostly-laminated structure. Also present in all cases are so-called deformation twins and high density dislocation clusters. Starting with 304L 2B300, we see in Fig. 3.3 that the microstructure is dominated by laminated structures which are probably plate-like. The laminar structures are highly anisotropic in dimensions

indicated by the frequency distribution for the grain size of the laminar spacing which shows an effectively unimodal distribution which confirms a uniform structural refinement (Fig. 3.4), with an average thickness (D1) of ~ 70 nm. The length of laminations averages at ~ 1.8 μm. The continuous ring in the selected area diffraction (SAD) pattern indicates a fine-grained polycrystalline microstructure with certain texture. All the laminations or "columns" appear to be oriented the same way as can be discerned by moving the viewing area around.

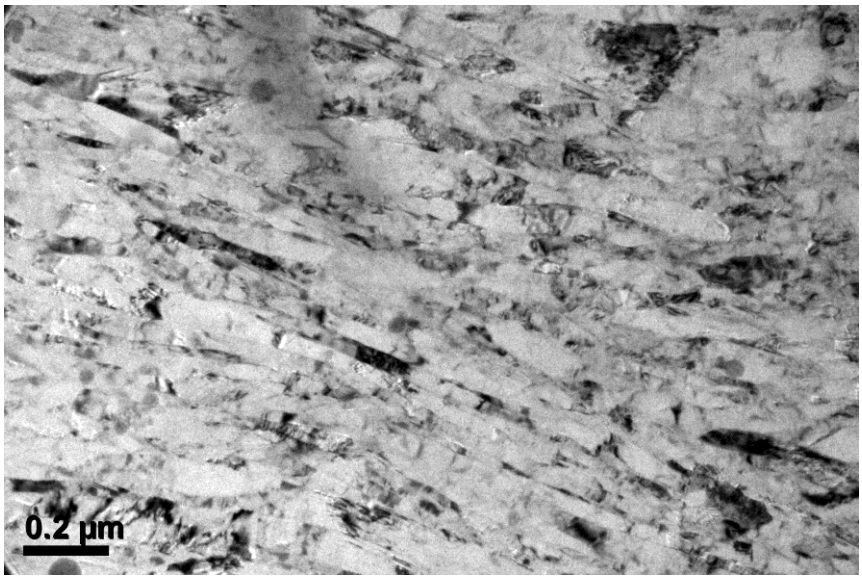

Fig. 3.3. - (A) 304L 2B 300 bright field TEM micrograph showing laminated grains along the transverse direction. (B) Selected area diffraction pattern (SAD) shows polycrystalline nature of grains with certain texture and predominant austenite structure

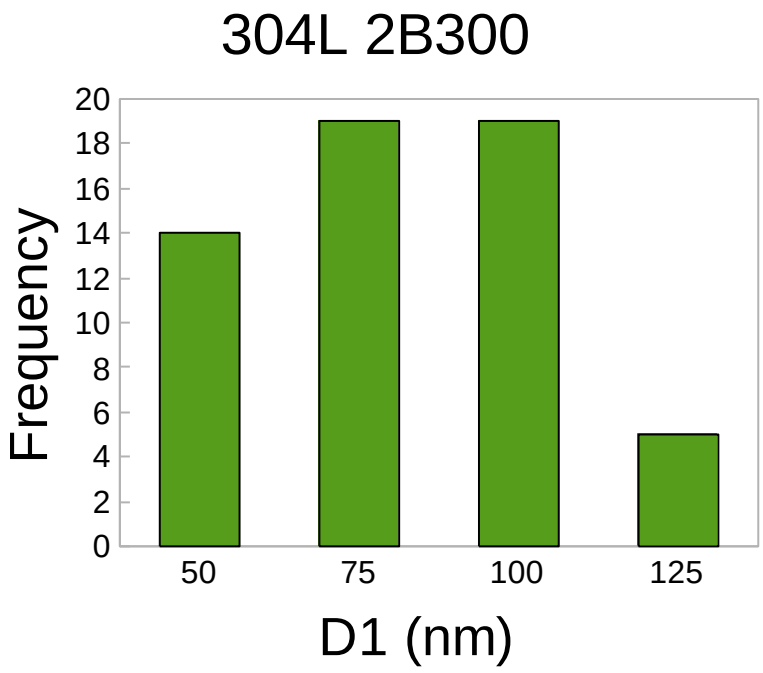

Fig. 3.4. - Frequency histogram of 304L 2B 300C specimen showing the unimodal character of laminar thickness with an average laminar thickness of ~ 70 nm

Further processing at higher temperature shows that the laminar structure remains, but the length of grains decrease significantly as shown in Fig. 3.5a. for the 304L 4Bc 500 specimen. The average laminar spacing increases slightly in order to accommodate the decrease in length. Average laminar spacing (D1) becomes ~ 120 nm while the longer dimension (D2) has an average length of ~250 nm with a bi-modal distribution, albeit with a noticeably smaller occurrence of larger grains. Furthermore, some equiaxed grains become apparent. The bi-modal distribution of D2 is indicative of the occurrence of grain columns being compressed as will be more apparent in the case of the six-pass material. After six passes, the 304L 6Bc 500 sample undergoes even further grain refinement as is evident by the frequency histogram in Fig. 3.6. The average laminar spacing now decreases slightly to ~ 100 nm, as shown in Fig. 3.7a, and the size distribution takes on a more obvious unimodal

characteristic which also implies that the threshold for grain refinement is being reached. Similarly, the longer dimension decreases further to an average size of ~ 260 nm, also with a unimodal type of distribution as presented in Fig. 3.7b. Upon close examination of the micrograph, more equiaxed grains can be discerned within the surrounding laminated grains. This is consistent with the original trend established in that the long grains are now being compressed in to smaller, equiaxed grains, which is also confirmed by the unimodal distribution.

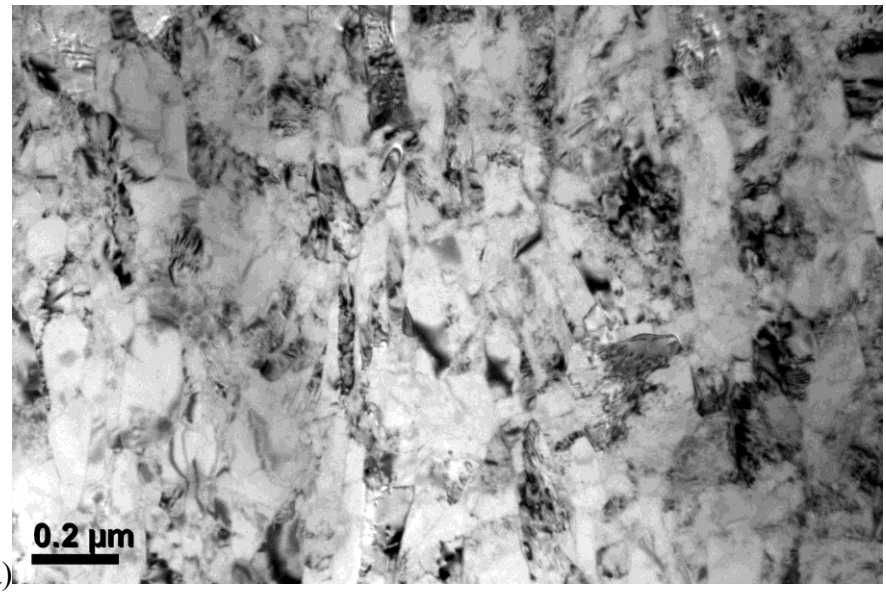

(a)

Fig. 3.5. - (A) 304L 4Bc 500 bright field TEM micrograph showing laminated grains and gradual formation of equiaxed grains along the transverse direction. (B) Frequency histogram of grain size showing a bimodal distribution indicative of long grains becoming smaller equiaxed grains. (C) Frequency distribution of long grain dimension indicating a decrease in laminar structure

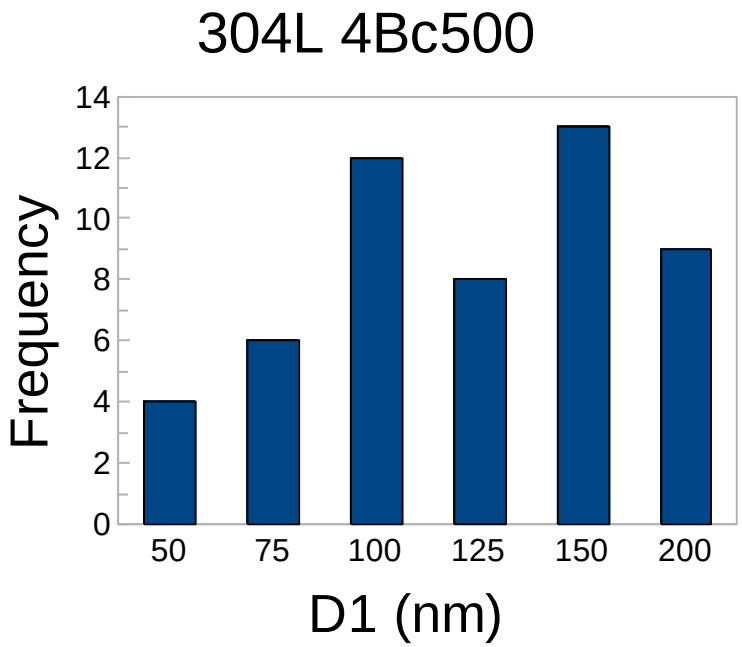

(b)

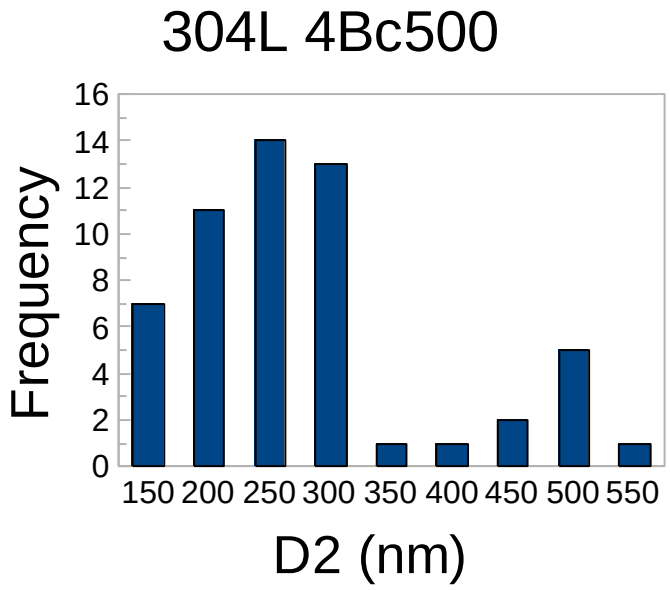

(c)

Fig 3.5 continued

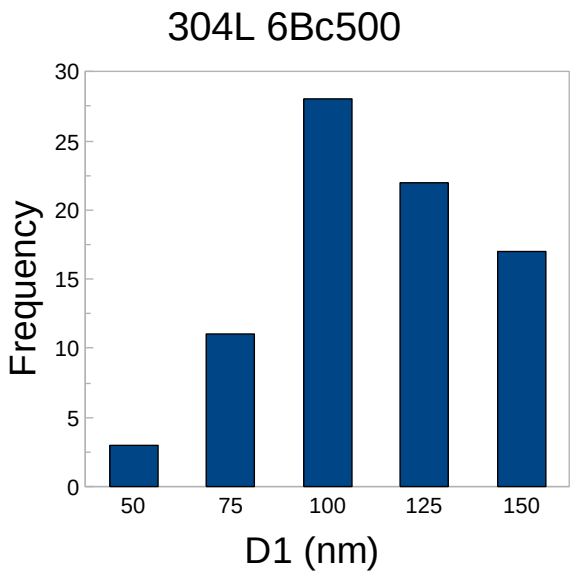

Fig. 3.6. - Grain size distribution of 6Bc 500 approaching unimodal character

A similar situation arises in 316L stainless steel. The 316L 2B 300 specimen shows a mostly-laminated structure along the transverse direction, Fig. 3.8a, with a unimodal average laminar spacing of ~ 80 nm as shown in Fig. 3.8b. The laminations also seem a little more randomly oriented than 304L 2B 300 which may contribute to the slightly higher hardness mentioned later in this section. However, unlike the previous 304L 2B 300 micrograph, this TEM sample was prepared via precision ion milling and so consequently, a much smaller viewing area is visible so it is difficult to get a notion of how long the grains are and also restricts the number of grains by which to base the distribution of grain size. However, it can be inferred by inspection that the grain extends through large areas of the sample just as in 304L 2B 300.

(a)

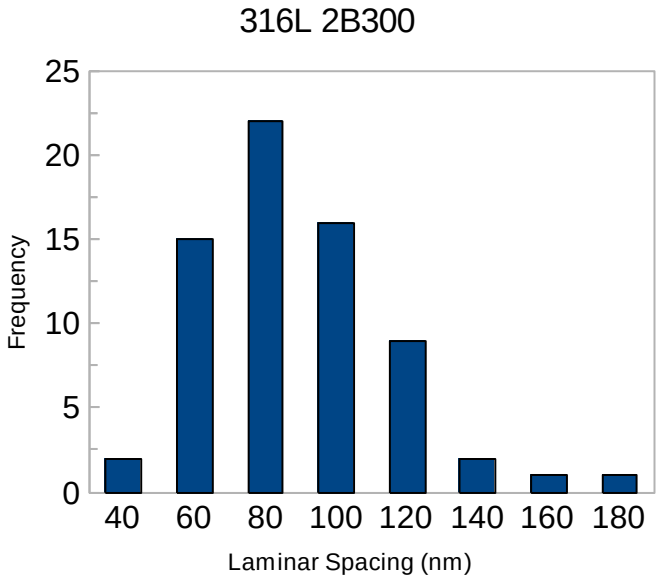

(b)

Fig. 3.7. - (A) Brightfield TEM micrograph of 316L 2B 300. (B) Frequency histogram of laminar thickness

Processing at higher temperature and greater passes, 316L 4Bc 500C, leads to an average laminar thickness of 80 nm. Unlike with the previous 304L micrographs, the

striations seem to run randomly through the viewing area rather than aligning in a common direction, which may also contribute to the observed hardness. The length of laminars has been dramatically reduced compared to the 316L 2B 300C specimen. This may in fact be an evidence of a tendency to form equiaxed grains after more ECAP extrusions. Indeed, the appearance of what may be equiaxed grains is apparent from the TEM micrograph in Fig 3.8 (a). This appearance persists throughout the entire viewing area and so indicates a uniformity of overall microstructural refinement.

(a) 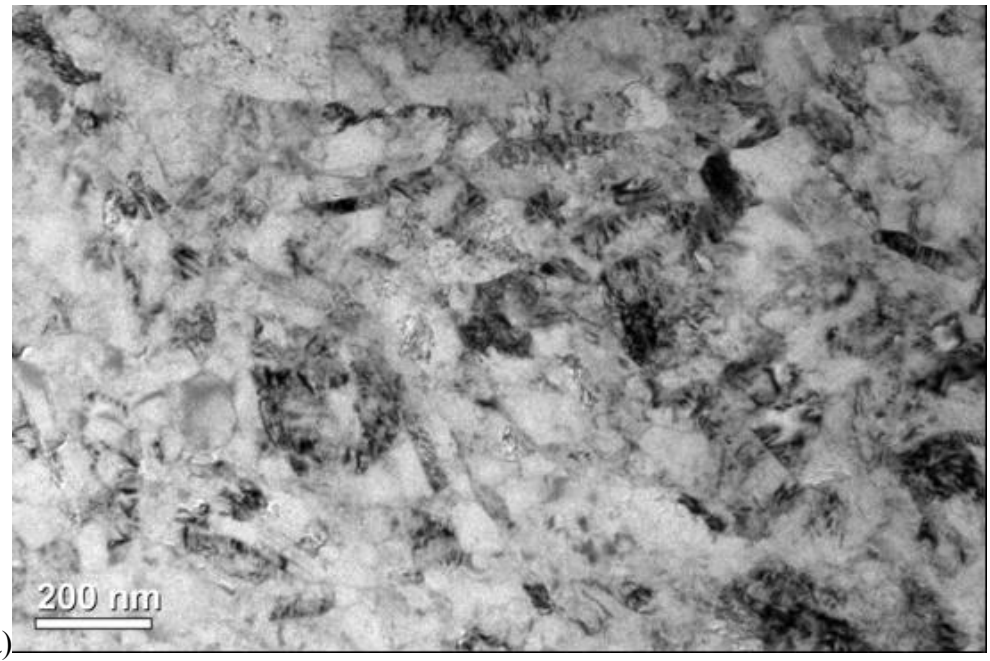

Fig. 3.8. - (A) Brightfield TEM micrograph of 316L 4Bc 500. (B) Frequency histogram of laminar thickness

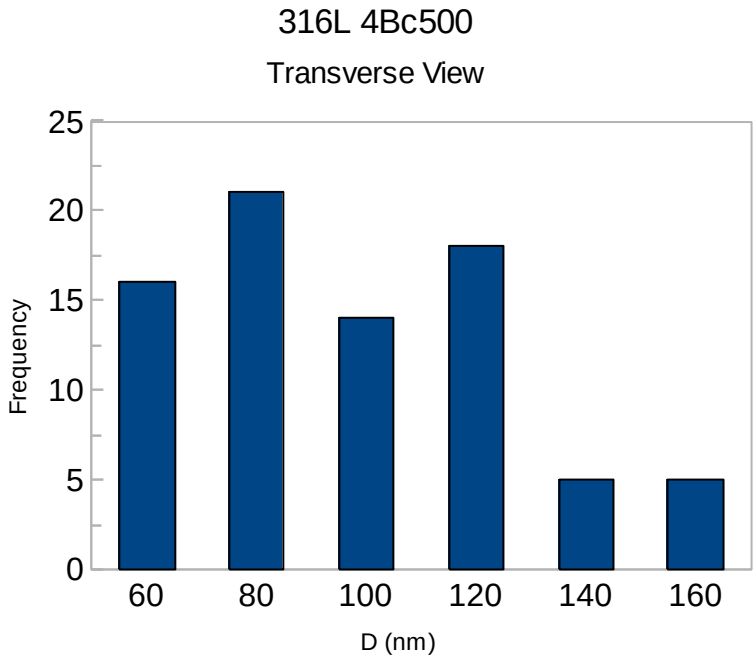

(b)
Fig 3.8 continued.

3.2. Mechanical Properties

3.2.1. Microhardness

The hardness evolutions of 304L and 316L before and after processing are summarized in Table 3.1. As expected, it can be seen that material hardening increases with further processing. In both 304L and 316L, significant hardening can be seen in their respective 1A RT processing. While this may be easily attributed primarily to the presence of martensite in 304L, it's slightly more difficult to account for in 316L considering the predominance of austenite with only a slight fraction of martensite. Hardness increases steadily with further processing at higher temperatures, however, which is consistent with the observed grain size refinement previously discussed. The hardness of 316L seems to increase faster than that of 304L since the hardness of 316L 4Bc 500 is comparable to that of 304L

6Bc 500. This strengthening trend will also be apparent in the results from tensile tests to be discussed later. Also displayed is a graph of hardness versus as-processed grain size for 304L. 316L is excluded due to lack of data points.

Table 3.1. – Hardness (H_{IT}) Evolution of ECAPed Samples

	SS 304L	SS 316L
Annealed	2.20 ± 0.05 GPa	2.10 ± 0.03 GPa
1A RT	5.70 ± 0.09 GPa	4.90 ± 0.12 GPa
2B 300	4.30 ± 0.09 GPa	4.60 ± 0.13 GPa
4Bc 500	4.80 ± 0.14 GPa	5.10 ± 0.16 GPa
6Bc 500	5.10 ± 0.17 GPa	N/A

3.2.2. Tensile Testing

Tensile testing results for only three ECAPed specimens are discussed because those were the only supplied as of this writing. Overall reduction in billet dimensions after subsequent processing limited the number of tensile test samples to two. The stress-strain curves (Fig. 3.9) for each processed material are presented and the yield stress and strain at fracture for each specimen are summarized in Table 3.2. Images of the actual tensile test samples after fracture were not provided so it is difficult to make further assessments on the nature of the fracture beyond that which can be inferred from the provided FESEM micrographs (Fig. 3.10) as well as a comparison of fractures from sample to sample. Also, those who provided the tensile test results note that sample geometries prevented the extensometer from being placed on them. Therefore the displacement between grips was measured manually and considered more accurate than crosshead displacement.

Table 3.2. Summary of Uniaxial Tensile Tests for 304L and 316L

Specimen	Strain Rate [s^{-1}]	Yield Stress [GPa]	Strain at Fracture
304L 4Bc 500	0.001	1.099	.31
304L 4Bc 500	0.01	1.210	.26
304L 6Bc 500	0.001	1.212	.19
304L 6Bc 500	0.01	1.285	.16
316L 4Bc 500	0.001	1.253	.16
316L 4Bc 500	0.01	1.284	.18

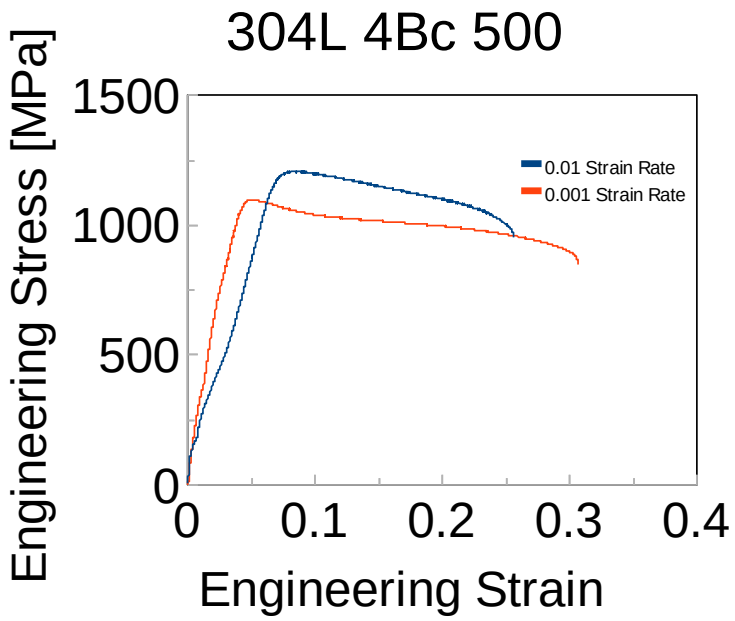

(a)

Fig. 3.9. - Stress-Strain curves for (a) 304L 4Bc 500 (b) 304L 6Bc 500 and (c) 316L 4Bc 500

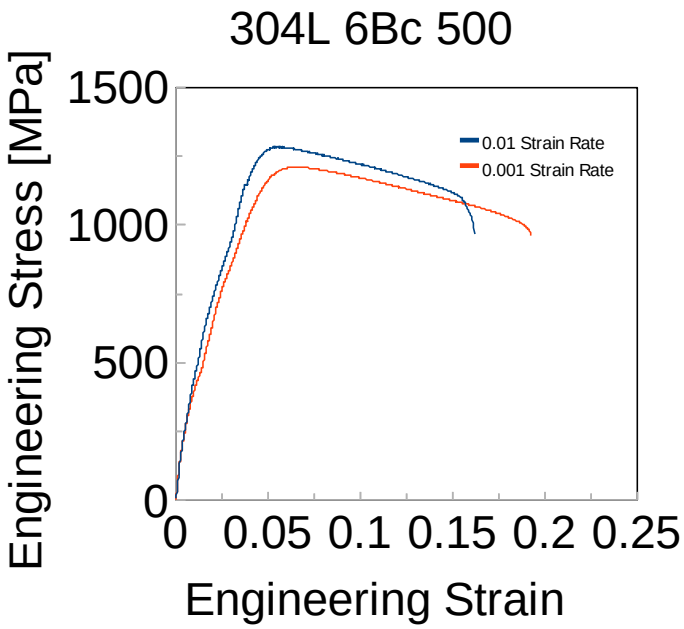

(b)

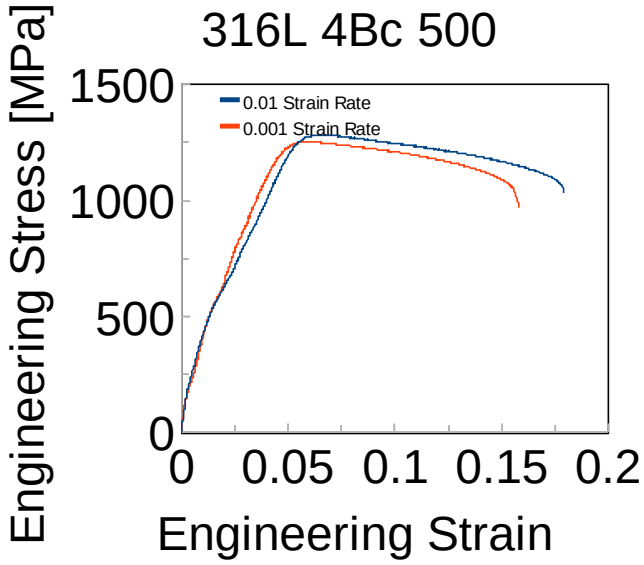

(c)
Fig. 3.9. continued

It can be seen that there is an increase in yield stress from 304L 4Bc 500 to 304L 6Bc 500. 304L 4Bc 500 appears to be the most ductile of all the specimens considering the high amount of strain it is able to withstand before fracture. It also appears to have a comparable

yield stress to those of 304L 6Bc 500 and 316L 4Bc 500. However, it is also important to note that there is a severe sensitivity to strain rate in this specimen as the yield stress decreases by about 200 MPa when the strain rate is reduced by a factor of ten. This strain rate dependence is also apparent in 304L 6Bc 500 albeit to a lesser degree implying that additional processing may also impart a tendency to lock the grains in to place. Interestingly, 316L 4Bc 500 has a comparable yield stress and fracture strain to that of the 6-pass 304L sample indicating that similar working is achieved in 316L by a lower number of passes when compared to 304L. Furthermore, there appears to be very limited strain rate sensitivity in 316L. Analysis of fracture surfaces for all specimens indicates a ductile fracture mode for both strain rates. Dimples become finer in 304L for specimens after a higher number of passes. The dimples in 316L 4Bc 500 are comparable to those of 304L 6Bc 500 confirmed by their comparable yield stresses and strain-at-fracture.

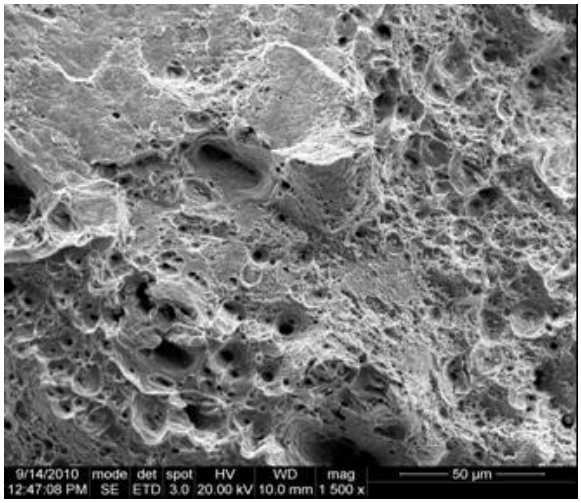

Fig. 3.10. - FESEM micrographs of the fracture surfaces of 304L 4Bc 500 ((a), (b)), 304L 6Bc 500 ((c), (d)), and 316L ((e), (f))

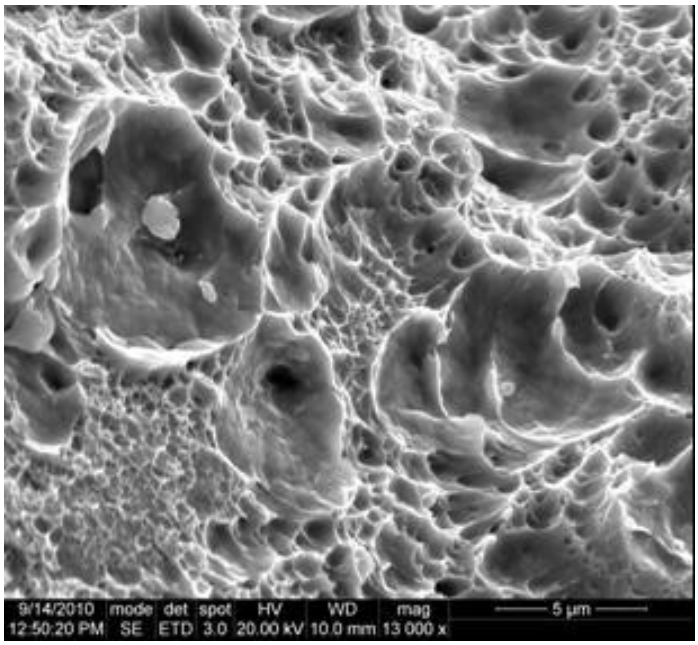

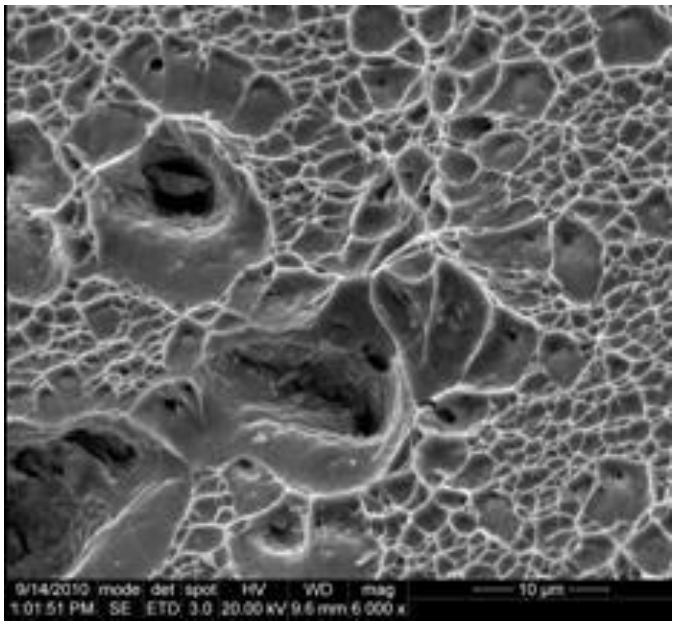

Fig. 3.10. continued

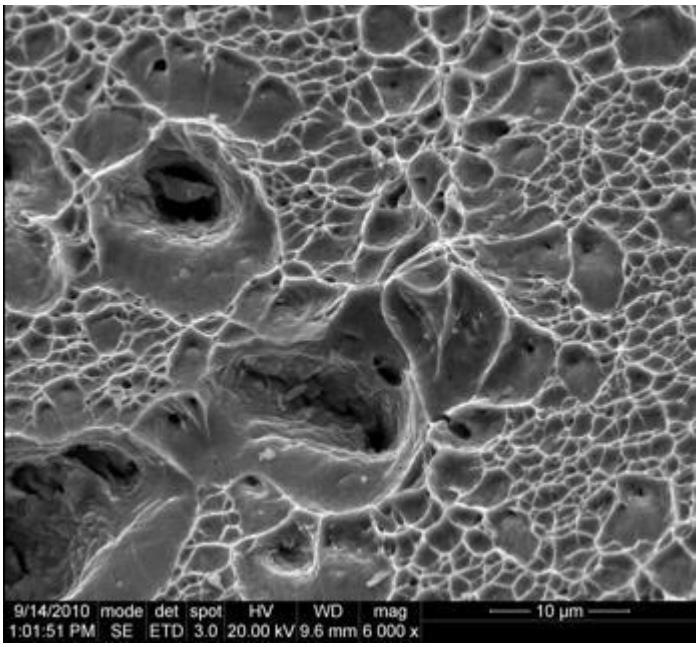

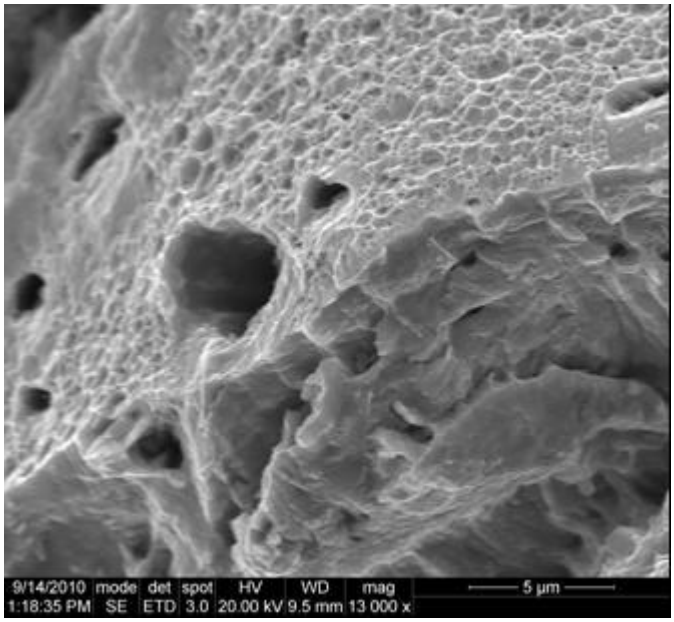

Fig. 3.10. continued

(f) 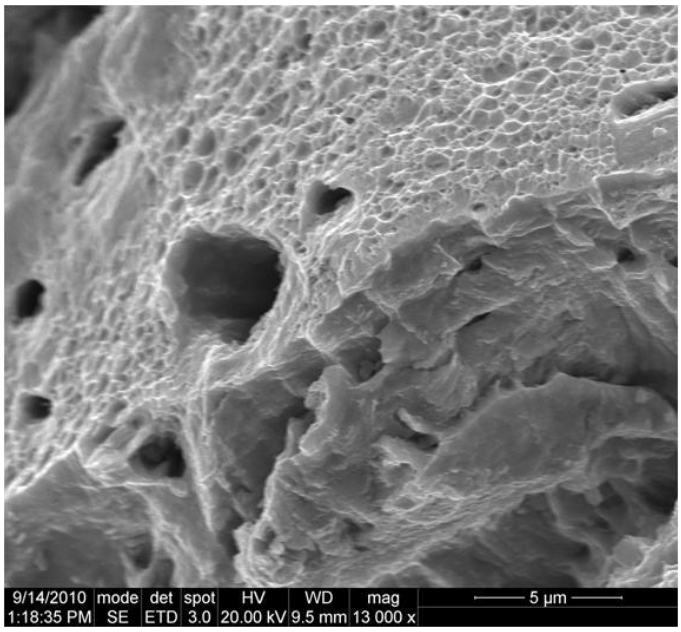

Fig 3.10 continued

3.3. Discussion

3.3.1 Microstructure

3.3.1.1. XRD

The appeal of X-Ray diffraction is its versatility while remaining a non-destructive and powerful technique to analyze the microstructure of materials. Our primary interest in using this technique is to characterize the effects of ECAP on the microstructure of our stainless steels. It's been reported in the literature that austenitic steels subjected to ECAP tend to form predominantly martensite phases after numerous Bc processing at room temperature [33]. Huang et al.. Report ~83% volume fraction of martensite after 8 passes following this route. An XRD plot of their results is shown in Fig. 3.11. It appears that there is probably a temperature dependence on this so-called deformation induced martensite transformation (DIMT) [34] since, our multiple passes (4 – 6) at higher temperature did not impart such a noticable or significant quantity of martensite as can be seen from, for example, the ECAP 4-pass specimen reported by Huang et al.. (Fig. 3.2.1). No mention of processing temperature was made in that study by Huang et al.., however it can be inferred that it was performed at lower temperatures than our sample based on our results for 304L.

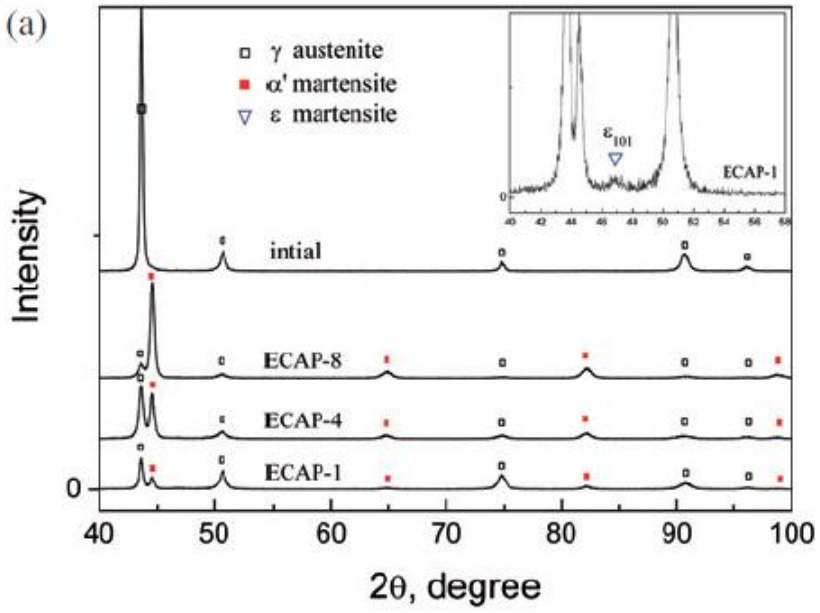

Fig. 3.11. - XRD of microstructural evolution of ECAP 304L as produced by Huang et al.

3.3.1.2. Formation of Fine Austenite Grains

Microstructural refinement is achieved primarily through the action of deformation twinning during severe plastic deformation. Plastic shear strain at the beginning of the ECAP process produces a high density of deformation twins. These twin boundaries subdivide the original grains in to thin plate-like grains whose thickness are in submicron regime while the length extends through much of the original coarse grains. Successive processing via ECAP further divides these grains due to shear deformation from different directions consequent of the 90^{o} rotations between passes. This happens because large dislocation clusters are introduced into the twin grains generated from the initial passes in order to accommodate further plastic strain. These dislocations develop in to grain boundaries via the action of additional ECAP processing. ECAP also allows for the formation of fine-grained austenite

grains via the mechanism of twin fragmentation. Grain refinement mechanisms transform from that of the dislocation division previously discussed to a so-called twin fragmentation mechanism. A limiting grain size refinement is restricted by factors such as stacking fault energy. A high-enough stacking fault energy tends to a fast dynamic recovery of dislocations during deformation. This prevents the dislocations from forming in to grain boundaries. It is unclear why we would witness less recovery of dislocations with processing at higher-than-room temperature. Twin boundaries also act as obstacles to dislocation recovery. As mentioned earlier, results from TEM show the formation of these platelets which gradually evolve in to equiaxed-looking grains.

3.3.2. Mechanical Properties

It is well known that nanocrystalline or fine grained materials exhibit superior mechanical properties. We see from our studies that the refined grains produce harder material with increases in yield stress and decreased sensitivity to strain rate. It is usually suspected that finer grains should also lead to increase in material ductility. Such was not the case in our study. We find that there is an overall decrease in ductility from samples of lesser processing to those of more. This is not totally unexpected since such heavy deformation due to our processing is not without artifacts such as pores and tensile instabilities [35], although this effect can be diminished by using tensile specimens of such small geometry as ours. This trade of ductility for yield stress in bulk materials should thus be expected. This may also support the notion that a high density of dislocations induced by processing may play a role in the grain refining process. The increase in hardness is expected with ECAPed material.

4. THERMAL STABILITY AND RADIATION TOLERANCE

The operating conditions within nuclear reactors places structural materials in rather extreme environments leaving them exposed to combinations of factors such as extreme temperatures, and high energy particle bombardment. While not comparable to the real thing, certain preliminary analysis can be used to establish a general trend of a material's response to these conditions. Thus we discuss ECAP material response to isochronal annealing and helium ion bombardment in this section.

4.1. Thermal Stability

4.1.1. Annealing

Isochronal annealing of ECAP processed material was performed for one hour on samples machined from the transverse plane of the billets with dimensions approximately 1 cm^2 and 1 mm thick. The annealing temperatures investigated were initially 400, 600, and 800^oC. The intermediate temperature 700^oC was decided after review of the initial annealing data in order to "fill in the data gaps" between 600^oC and the sharp drop in hardness at 800^oC. All samples were then allowed to cool to room temperature in the open air. Hardness (H_{IT} at constant loading rate) was again measured for all annealed samples and compared with those of their as-processed representatives. The charts in Fig. 4.1 summarize the hardness recorded for the as-annealed samples, and provide one way to discern isochronal thermal stability of ECAP material at elevated temperature.

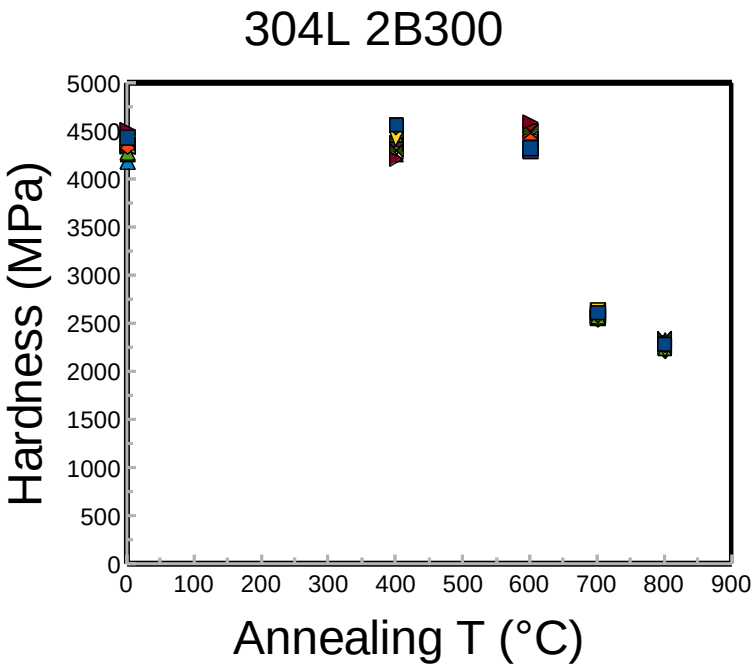

(a)

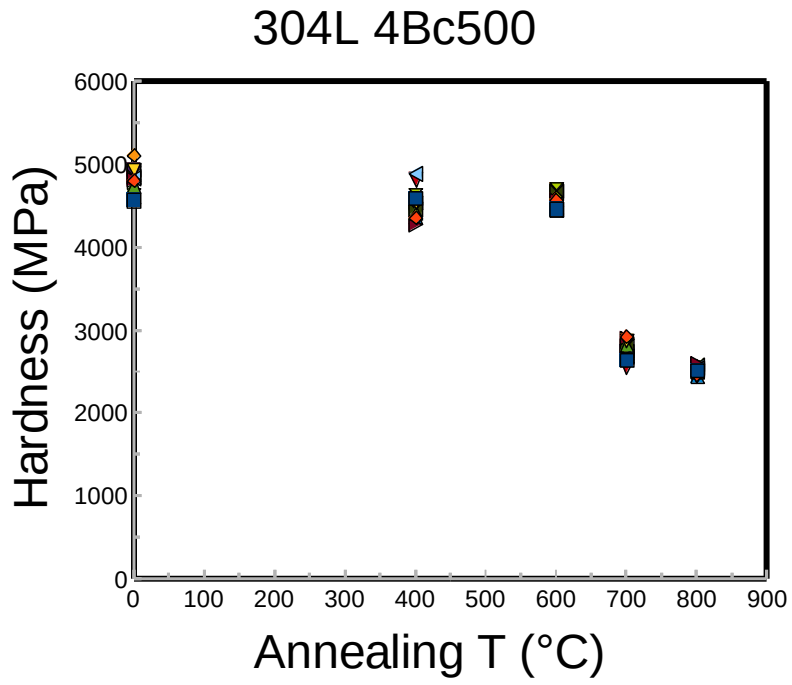

(b)

Fig. 4.1. - Isochronal annealing curves for as-processed 304L (a) 2B 300, (b) 4Bc 500, and (c) 6Bc 500

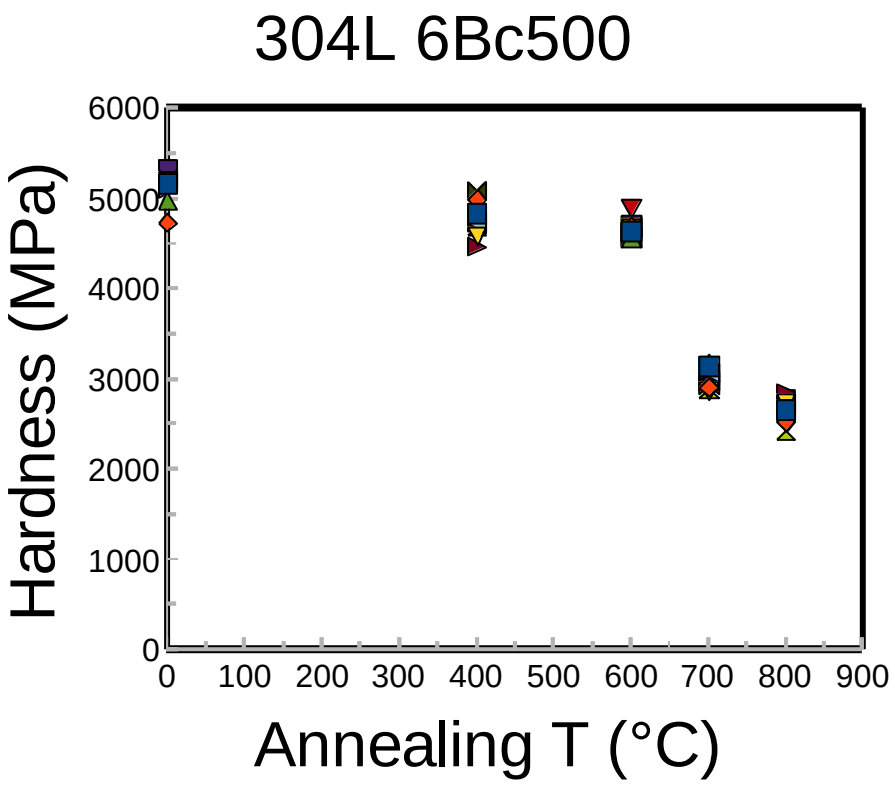

(c)

Fig 4.1. continued

The similar trends in these charts suggest that the microstructure of ECAP-processed material is stable at least up to 600^{o}C, for at least an hour regardless of processing history and temperature. The stability at this temperature is better than Fe-14Cr-16Ni model alloy where there are no other impurities. Lack of material prohibited studies of intermediate temperature between 600 and 700^{o}C, however, but it is clear that any sense of thermal stability rapidly diminishes in that range. These observed trends may give an optimistic outlook for the thermal stability of ECAP austenitic stainless steels in temperature ranges up to 600^{o}C regardless of ECAP processing history. More thermodynamic details regarding this system

are pending differential scanning calorimetry (DSC) investigation and microstructure analysis using TEM.

4.2. Radiation Damage

4.2.1. SRIM Simulation

The design of irradiation experiments is largely influenced by results of simulation calculations. Stopping and Range of Ions in Matter (SRIM) is the protocol used in this study. SRIM considers most aspects of energy loss in matter and the software includes quick calculations which produce tables of stopping powers, range, and damage distributions for an ion at an energy on to any target (elemental or mixture of elements as in an alloy). The interest at this stage in the research is in He ions and so these are considered for energies 100 keV. The simulation is calculated for a target with similar percent composition for iron, chromium, and nickel only. Minor alloying elements such as phosphorous and carbon were not considered. Moreover, a theoretical density was calculated from the weighted averages of the alloying elements. This simulation also assumes an amorphous target, so that there is no theoretical consideration for the crystalline microstructures of the material under investigation and so, are independent of processing history. The parameters are as follows: the target is assumed to be normal to the incidence beam and the number of incident ions is 10,000. The thickness is set for 1.5 microns as the penetration depth is seldom more than a few hundred nanometers. The raw outputs from the software are insufficient for the design of our experiments. A useful parameter in the study of radiation damage of solids is the so-called displacement-per-atom (DPA). DPA is a measure of the average number of displacements of lattice atoms due to interactions of incident energetic particles with atoms

(and also atoms with other displaced atoms). A graph of DPA vs. penetration depth reveals a distribution of damage region as a function of depth. In this way a peak-damage region, rather than just a maximum penetration depth, can be predicted. Knowing the peak damage region strongly aids in the analytic portion of the overall project. Investigation of the cross-section by TEM requires that this region be known to a very close approximation lest the peak-damage region be destroyed or altogether missed during sample preparation and microscopy. Additionally, microhardness measurements as a function of depths and including the peak damage region, allow enough room to get accurate measurements of radiation hardness without accidentally indenting beyond the damage region. Though DPA is not an output parameter from the software used, simple calculations based on other output data easily give a corresponding DPA which can be plotted against the penetration depth. So, for given energy and ion flux (dose), the following DPA vs. depth profiles are generated for "304L" and "316L" stainless steels at given doses and energy.

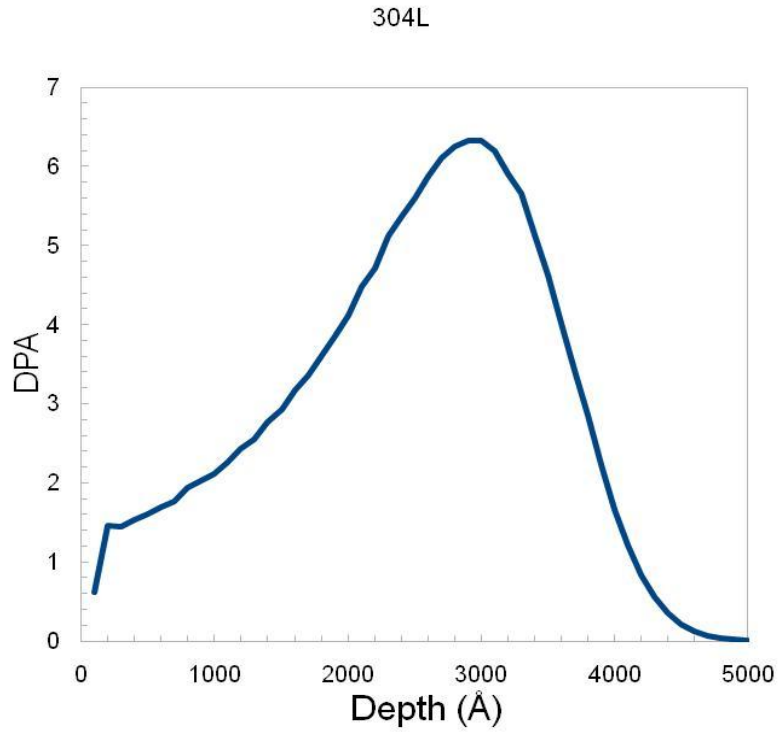

(a)

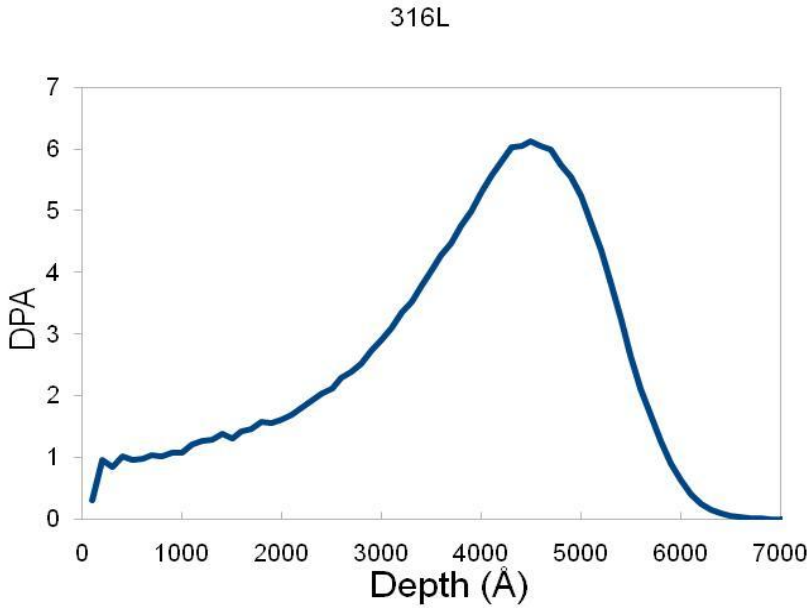

(b)

Fig. 4.2. – 100 keV He^{+}/6.0x10^{16} ions/cm^{2} SRIM outputs for approximately (a) 304L and (b) 316L

The charts for 100 keV (Fig. 4.2) indicate that the region of maximum damage should be somewhere around 300 nm deep in from the radiated surface of “304L”. So it is this region and the few hundreds of nanometers around it which will be treated in the next section on radiation hardening. The output for “316L” suggests that the slight variation in Ni and Cr is enough to change the damage profile as it predicts a deeper peak damage region at ~ 450 nm.

4.2.2. Radiation Damage and Hardening

Sections of as-processed material were machined from the transverse plane of the billets as previously discussed. The sections were ground and polished in the standard metallographic way with an additional final polish via vibration polishing and 20 nm silica polishing suspension. A two-dimensional raster scan by a Dektak 150 profilometer confirmed that the material had an overall roughness of approximately 20 nm which is the limitation of surface finish achievable by this author. Our electro-polishing technique has, as of yet, not been refined enough to give a smoother finish. A 20 nm finish should nevertheless be sufficient as SRIM had already predicted a peak damage region well below this depth. The actual ion implantation is not performed by this author but instead by a user of a separate facility. In the interest of time, this author was persuaded to try to fit as many samples on the sample holder so as to minimize the number of implantation procedures and so reduce the amount of operation time. This resulted in a rather small irradiated area but which is nonetheless large enough to get some valuable insight on to the material's response to the radiation, particularly in localized hardness change. Extra care in the handling and mounting of irradiated samples was necessary in order to preserve the finish and the radiated area. Any careless treatment could destroy or at least distort the region of interest and give a false sense

of the hardness trends. Microhardness measurements were performed using the same technique as before. The only difference is in the programming of the measurement. Whereas it had been sufficient to indent at only a constant rate, these experiments require that the maximum indention depth also be controlled within the limitations of the instrument. So, a series of hardness tests at different maximum indentation depths follows. There are 12 indents per depth and the depths range from 150 to 500 nm in 50 nm steps. Additionally, these experiments are repeated on the as-processed material in order to get a baseline and establish the hardness increase. These results are reported in the following graphs. It can be seen that as 304L approaches the 6-pass condition, the spacing or increase in hardness from as-processed to irradiated decreases and, in fact, overlaps. The results are shown in Fig. 4.3.

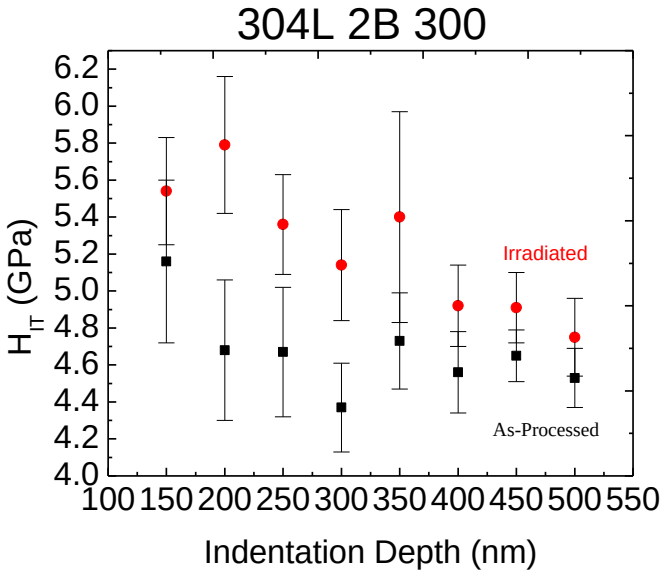

(a)

Fig. 4.3. - Indentation hardness of 100 keV He-irradiated material versus as-processed as a function of indentation depth. (a) 304L 2B 300, (b) 304L 4Bc 500, and (c)304L 6Bc 500

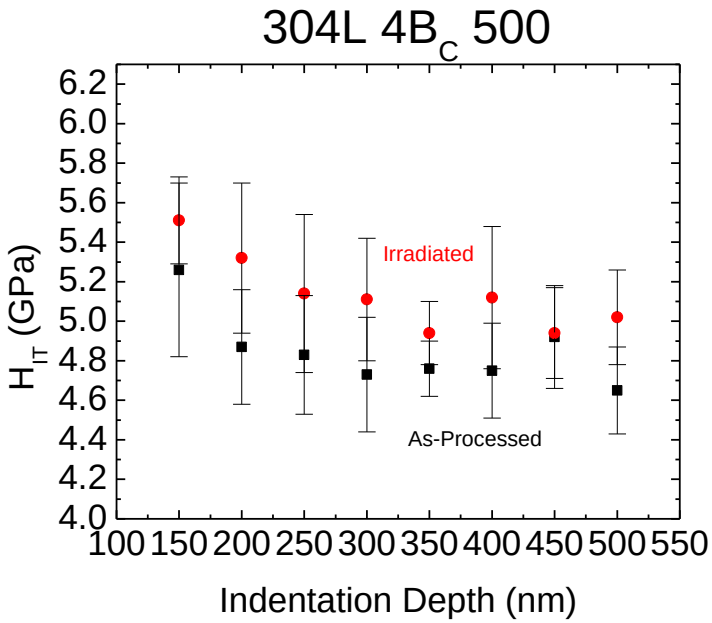

(b)

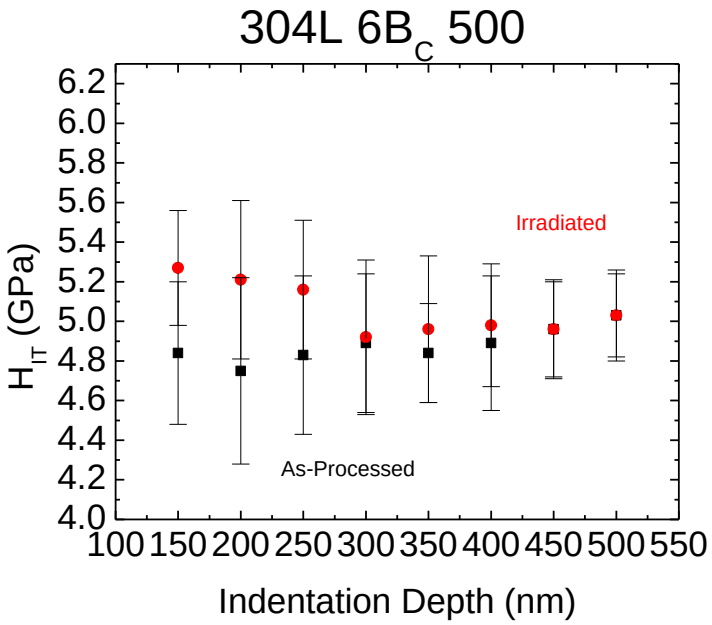

(c)

Fig 4.3. continued

Irradiation hardness change, ΔH_{IT}, as a function of average grain size, d, is also reported in Fig. 4.4.

It may seem that the smallest average grain size, ~70 nm, shows the most hardening, contrary to expectations. This indicates that it is not sufficient to assume that a "smallest grain dimension" is sufficient for enhancing radiation tolerance, but rather, there is dependence on overall grain morphology as the ~70 nm specimen is accompanied by grain lengths on the order of microns (compare with hardness evolution plot in Section 3). Unlike the predictions in SRIM, the peak damage region seems to be within the 200 – 250 nm range as this is where most of the hardness increase and spread is observed before leveling off in to a plateau. As a qualitative demonstration, a loading/unloading curve for one of the samples is shown contrasting the hardness change in Figures 4.5, 4.6 and 4.7.

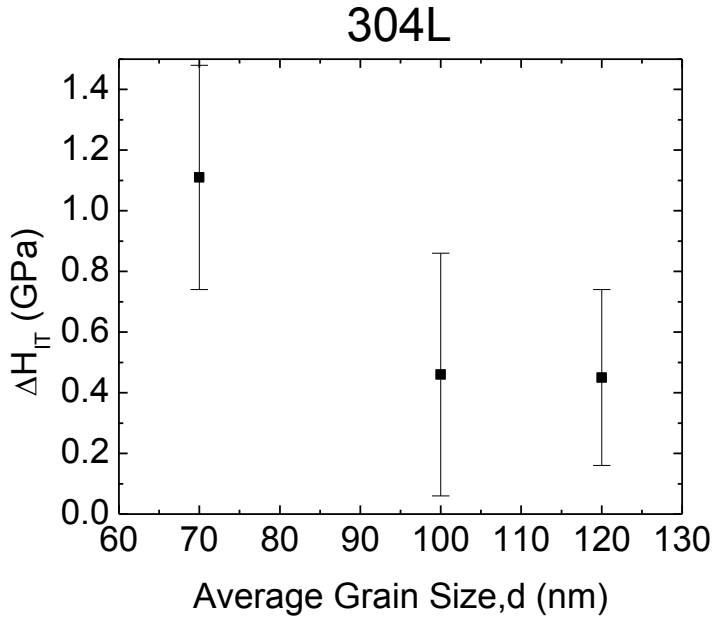

(a)

Fig. 4.4. - Indentation hardness change due to 100 keV He irradiation of as-processed 304L SS for average grain size, d, (a) and 1/d1/2 (b)

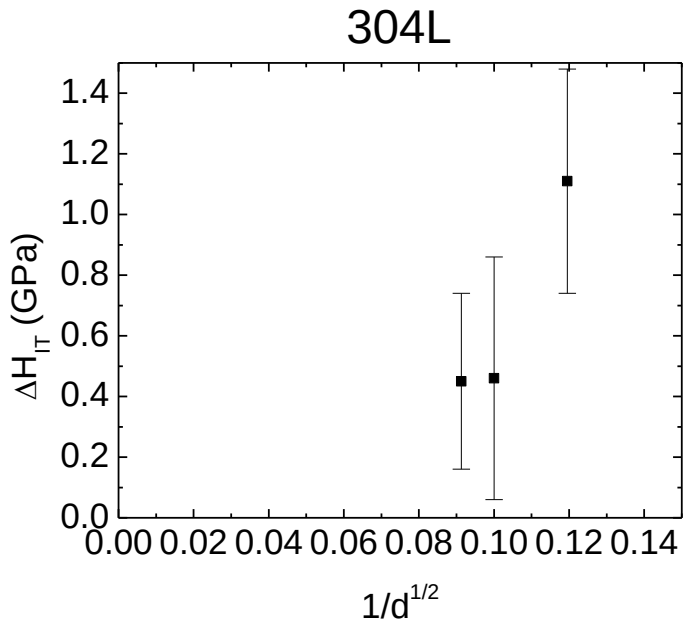

(b)

Fig 4.4. continued

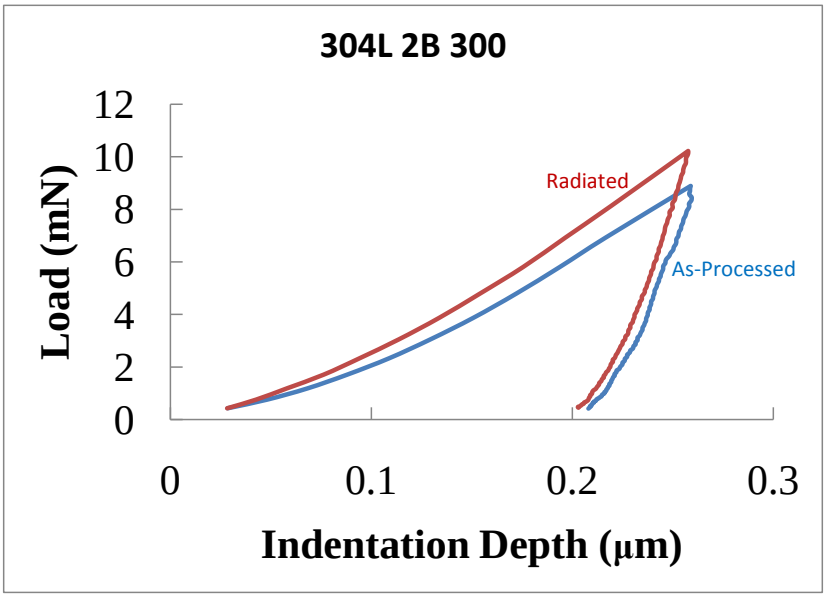

(a)

Fig. 4.5. - Loading/unloading curve for irradiated and as-processed 304L 2B300 at (a) 250nm indentation depth and (b) 350nm indentation depth

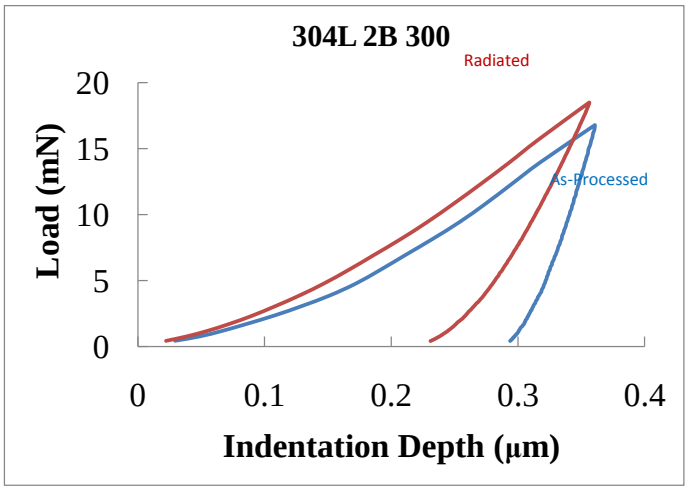

(b)

Fig. 4.5 continued

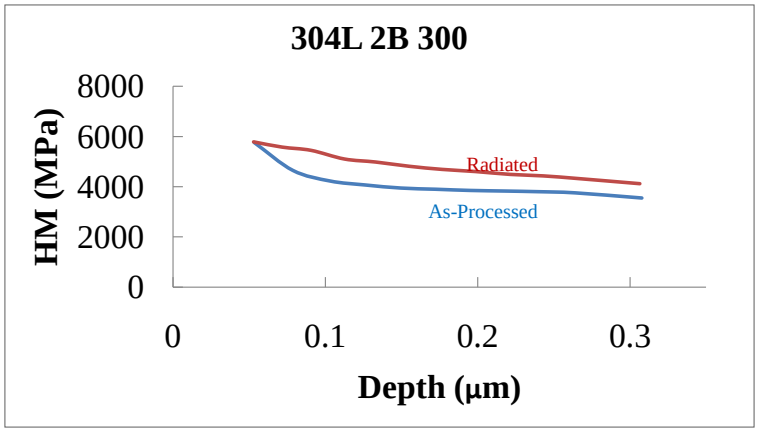

(a)

Fig 4.6. - Martens hardness (HM) vs. indentation depth for 304L 2B 300 (a) 300nm maximum depth and (b) 400 nm maximum depth

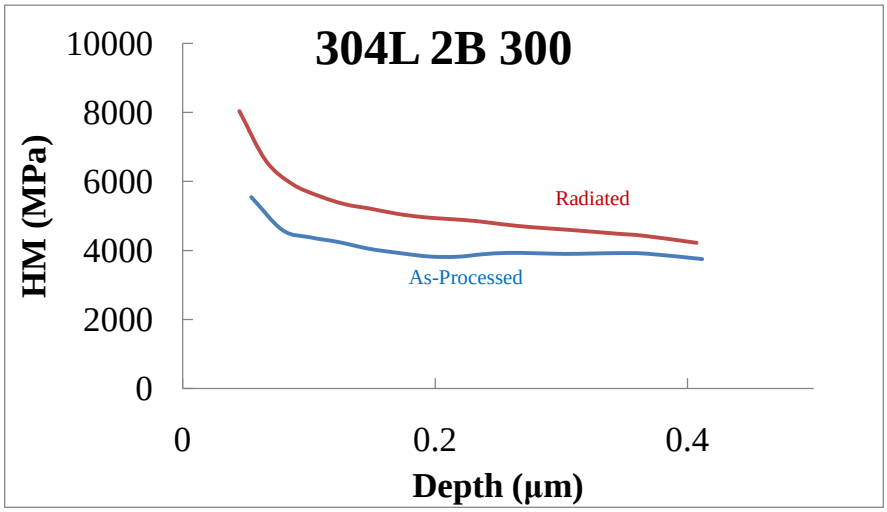

(b)

Fig. 4.6 continued

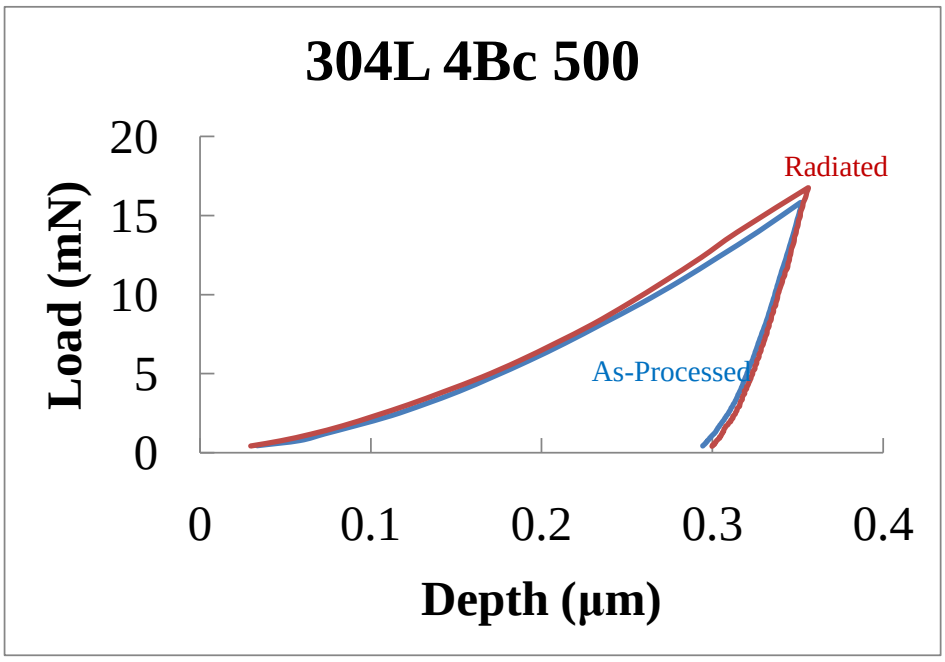

Fig. 4.7. – Loading/unloading curves and HM vs. depth curves for as-processed and radiated material

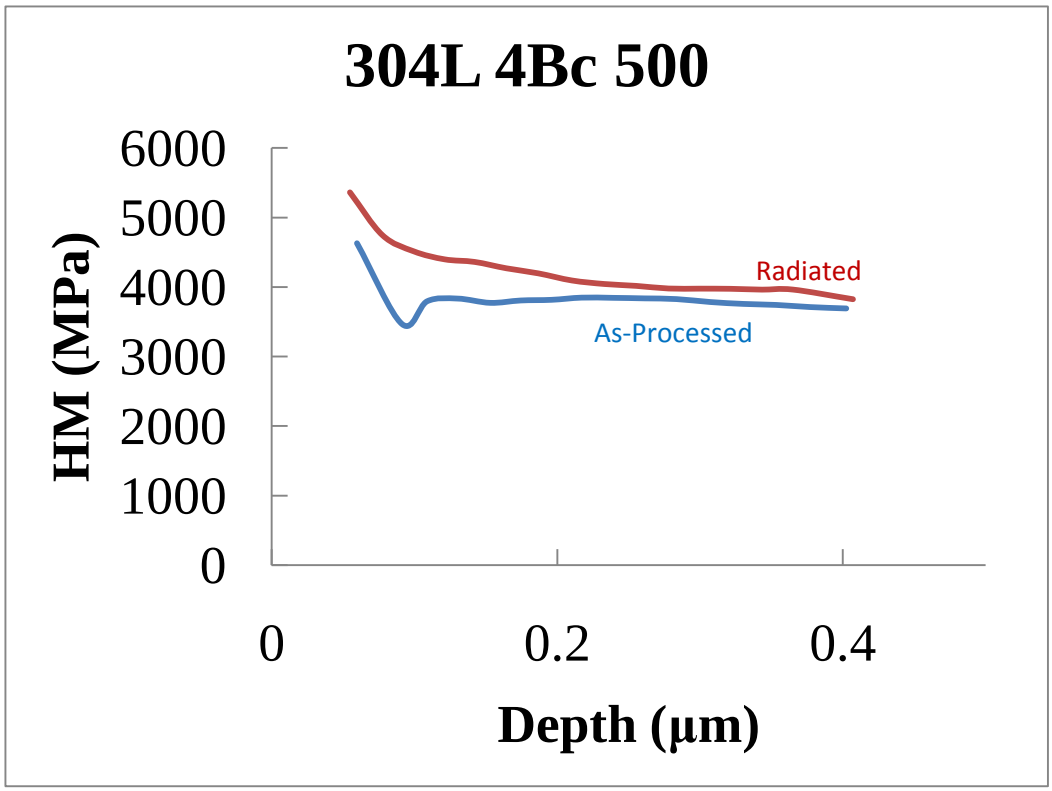

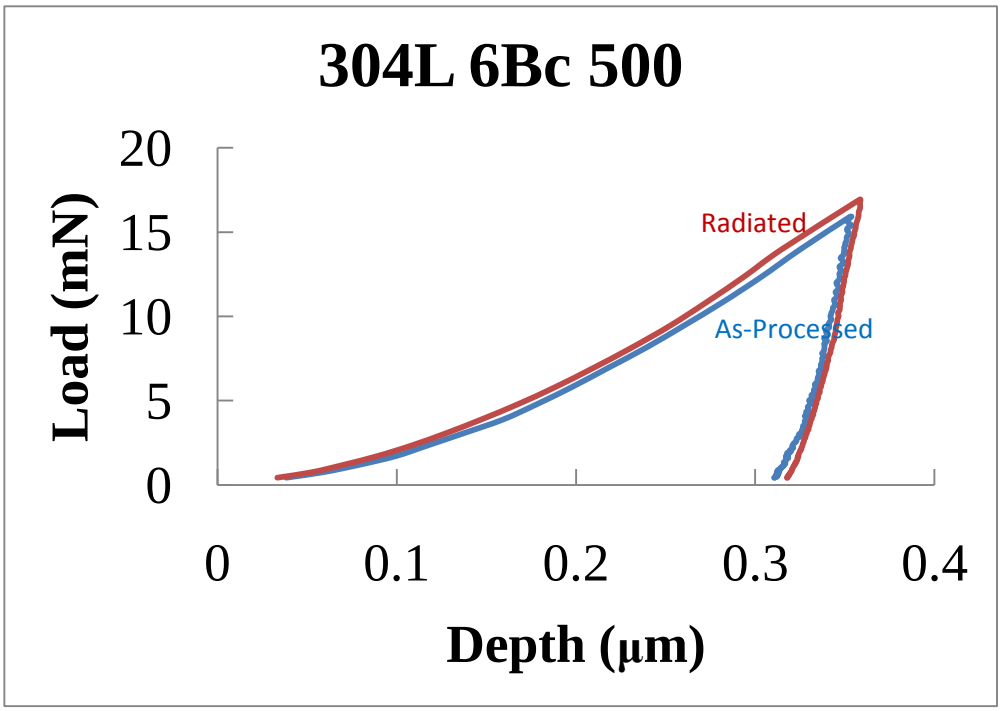

Fig. 4.7. continued

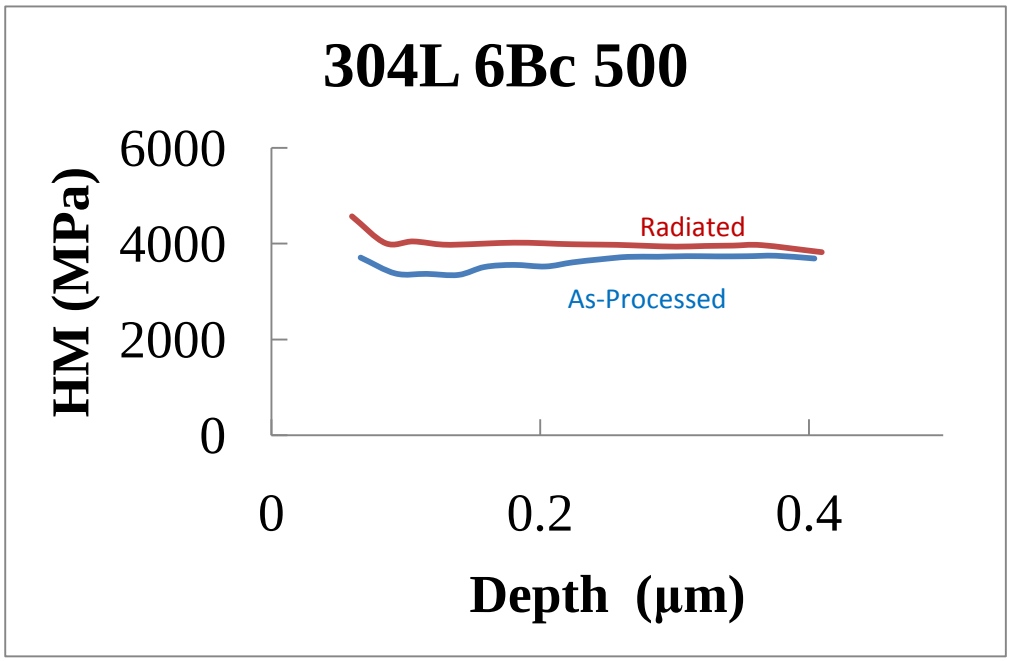

Fig 4.7. continued

4.3. Discussion

4.3.1. Thermal Stability

The ultra-fine grained 304L and 316L SS produced by ECAP seem to exhibit a degree of stability at least when held at 600^{o}C up to an hour. There is a marginal and barely noticeable decrease in hardness up to that point which may be due to recovery as some dislocations may have been absorbed in to the grain boundaries as has been previously reported [36]. An investigation in to the annealed microstructure would yield insight in to the nature of the grain growth. Moreover, isochronal annealing is in itself insufficient to describe the stability of the material. An in depth study in to the grain growth kinetics (if any) would require isothermal annealing experiments. At that point the grain growth kinetics can be described by

$$d^{1/N} - d_0^{1/N} = K_0 t \exp\left(-\frac{Q}{RT}\right) \quad (12)$$

where d is the grain size at a given annealing time, d_0 is the initial grain size, N is the grain growth exponent, K_0 is the kinetic constant, t is the annealing time, Q is the activation energy for grain growth and RT has its usual thermodynamic meaning. A logarithmic plot of such data could aid in the determination of the grain-growth exponent. As of now, application of SPD materials is limited since much internal energy is accumulated during the process. In order to be put to use, a lot of these materials may first need to undergo various heat treatments. It is thus necessary to understand isothermal behavior in order to discern whether or not these ECAP fabricated materials retain their mechanical superiority during treatments and/or service conditions.

4.3.2. Radiation Damage and Hardening

These trends indicate that radiation tolerance increases with a higher number of ECAP passes (possibly due to grain refinement [18],[32]), but the degree to which it ultimately does is yet to be determined since a baseline has not been established for the pre-worked material. This thesis author had attempted to fill in this gap, but was thwarted a number of times and so this has yet to be determined. Nevertheless, we may be able to get some insight into the nature of this radiation induced behavior. A study of the irradiated microstructure is also pending and is the most crucial for understanding the mechanism by which the changes in mechanical behavior occur. Nevertheless, it is believed that He-radiation hardening is not due to displacement of atoms alone but due largely to the concentration of He bubbles induced in the matrix. He bubbles may affect hardness in one or

both of two ways. As discussed by Hunn et al.., implanted He acts in such a way as to pin the dislocation loops created as a result of the radiation damage. Implanted He also acts as a direct barrier to the movement of dislocations. The stress required to initiate dislocation motion is given by

$$\sigma = \frac{\mu b}{l} \tag{13}$$

This observation agrees with the higher hardness reported near the expected peak damage region where there is likely to be the highest concentration of He atoms ("bubbles"). A combination of isothermal in-situ annealing and TEM experiments may shed some light in to the behavior of these He bubbles in our irradiated material as well as further insight in to how such generated defects contribute to or affect the microstructure during service temperatures. Also, the studies of Hunn et al.. also suggest that there may be a dependence on dose and temperature [4]. These current studies only concerned fix dose at fix temperature (room temperature). According to Mansur et al.., the helium generation and diffusion rates control helium buildup in cavities and thus affect both swelling and grain boundary embrittlement. It was widely believed that a gas like helium would have little effect on precipitation since it is chemically inert. But it was shown that helium actually causes changes in precipitation during irradiation [3],[7],[5],[10].

5. CONCLUSIONS

Nanocrystalline microstructures have successfully been fabricated in commercial AISI type 304L and 316L stainless steel. 304L was successfully ECAPed up to 6Bc passes at 500^{o}C while 316L was successfully processed to 4Bc passes at 500^{o}C. Not only is there a 2.5-fold increase in hardness, but there is also a tendency towards the achievement of equiaxed grains with subsequent ECAP pressing. With increasing ECAP passes, the load required for successful extrusion increases up to a maximum and then shows a decrease indicating a possible saturation of grain refinement or cold working. A notable result is that a predominant austenite structure is retained throughout subsequent ECAP presses at higher temperatures for both materials, as compared with materials ECAPed at room temperature in this study and throughout the literature which tend to develop predominant martensite structures. The trend of equiaxxing of grains is more easily observable via bright field TEM in the 304L specimen which shows first a laminated grain structure with ~70-nm laminar thickness tending towards a unimodal distribution of equiaxed grains ~100 nm in size. 316L seems to approach this regime faster as the ~80-nm striations of the 2B material evolves in to an equiaxed structure with ~100-nm grains. Tensile test data reflects hardening due to grain refinement and dislocation density by showing an increase in UTS with subsequent ECAP processing accompanied by a decrease in ductility. Additionally there appears to be a decreased dependence on strain rate in 316L versus 304L SS. ECAP processed materials are shown to be thermally stable up to 600^{o}C for up to an hour, after which it shows a rapid decline in hardness comparable to the annealed starting material. ECAP specimens were then subjected to 100 keV He-ion irradiation. Though nothing is conclusive as of yet, at least

preliminary hardness tests seem to indicate that the finer, equiaxed grains produced by subsequent ECAP passes show a marked reduction in radiation-induced hardening. This at least can paint a relatively optimistic picture for these materials for future studies and applications.

REFERENCES

[1] T.R. Allen, G.S. Was, S.M. Bruemmer, J. Gan, S. Ukai, Design of Radiation-Tolerant Structural Alloys for Generation IV Nuclear Energy Systems, in, 2005, pp. Medium: ED

[2] B.N. Singh, S.J. Zinkle, Defect accumulation in pure fcc metals in the transient regime: a review, Journal of Nuclear Materials, 206 (1993) 212-229.

[3] L.K. Mansur, E.H. Lee, P.J. Maziasz, A.P. Rowcliffe, Control of helium effects in irradiated materials based on theory and experiment, Journal of Nuclear Materials, 141-143 633-646.

[4] J.D. Hunn, E.H. Lee, T.S. Byun, L.K. Mansur, Helium and hydrogen induced hardening in 316LN stainless steel, Journal of Nuclear Materials, 282 (2000) 131-136.

[5] E.H. Lee, J.D. Hunn, T.S. Byun, L.K. Mansur, Effects of helium on radiation-induced defect microstructure in austenitic stainless steel, Journal of Nuclear Materials, 280 (2000) 18-24.

[6] G.E. Lucas, The evolution of mechanical property change in irradiated austenitic stainless steels, Journal of Nuclear Materials, 206 (1993) 287-305.

[7] E.H. Lee, T.S. Byun, J.D. Hunn, K. Farrell, L.K. Mansur, Origin of hardening and deformation mechanisms in irradiated 316 LN austenitic stainless steel, Journal of Nuclear Materials, 296 (2001) 183-191.

[8] T.S. Byun, K. Farrell, E.H. Lee, J.D. Hunn, L.K. Mansur, Strain hardening and plastic instability properties of austenitic stainless steels after proton and neutron irradiation, Journal of Nuclear Materials, 298 (2001) 269-279.

[9] T.S. Byun, K. Farrell, Irradiation hardening behavior of polycrystalline metals after low temperature irradiation, Journal of Nuclear Materials, 326 (2004) 86-96.

[10] N. Li, E.G. Fu, H. Wang, J.J. Carter, L. Shao, S.A. Maloy, A. Misra, X. Zhang, He ion irradiation damage in Fe/W nanolayer films, Journal of Nuclear Materials, 389 (2009) 233-238.

[11] S.J. Zinkle, B.N. Singh, Microstructure of neutron-irradiated iron before and after tensile deformation, Journal of Nuclear Materials, 351 (2006) 269-284.

[12] H. Trinkaus, B.N. Singh, Helium accumulation in metals during irradiation - where do we stand?, Journal of Nuclear Materials, 323 (2003) 229-242.

[13] V.M. Segal, Materials processing by simple shear, Materials Science and Engineering A, 197 (1995) 157-164.

[14] V.M. Segal, Severe plastic deformation: simple shear versus pure shear, Materials Science and Engineering A, 338 (2002) 331-344.

[15] Y.T. Zhu, T.C. Lowe, Observations and issues on mechanisms of grain refinement during ECAP process, Materials Science and Engineering A, 291 (2000) 46-53.

[16] R.Z. Valiev, T.G. Langdon, Principles of equal-channel angular pressing as a processing tool for grain refinement, Progress in Materials Science, 51 (2006) 881-981.

[17] L.R. Cornwall, K.T. Hartwig, R.E. Goforth, S.L. Semiatin, The equal channel angular extrusion process for materials processing, Materials Characterization, 37 (1996) 295-300.

[18] X.-M. Bai, A.F. Voter, R.G. Hoagland, M. Nastasi, B.P. Uberuaga, Efficient Annealing of Radiation Damage Near Grain Boundaries via Interstitial Emission, Science, 327 (2010) 1631-1634.

[19] D.H. Shin, J.-J. Pak, Y.K. Kim, K.-T. Park, Y.-S. Kim, Effect of pressing temperature on microstructure and tensile behavior of low carbon steels processed by equal channel angular pressing, Materials Science and Engineering A, 325 (2002) 31-37.

[20] D.H. Shin, I. Kim, J. Kim, K.-T. Park, Grain refinement mechanism during equal-channel angular pressing of a low-carbon steel, Acta Materialia, 49 (2001) 1285-1292.

[21] D.H. Shin, B.C. Kim, K.-T. Park, W.Y. Choo, Microstructural changes in equal channel angular pressed low carbon steel by static annealing, Acta Materialia, 48 (2000) 3245-3252.

[22] D.H. Shin, B.C. Kim, Y.-S. Kim, K.-T. Park, Microstructural evolution in a commercial low carbon steel by equal channel angular pressing, Acta Materialia, 48 (2000) 2247-2255.

[23] H.S. Kim, M.H. Seo, S.I. Hong, Plastic deformation analysis of metals during equal channel angular pressing, Journal of Materials Processing Technology, 113 (2001) 622-626.

[24] S.L. Semiatin, D.P. DeLo, E.B. Shell, The effect of material properties and tooling design on deformation and fracture during equal channel angular extrusion, Acta Materialia, 48 (2000) 1841-1851.

[25] N. Saito, M. Mabuchi, M. Nakanishi, I. Shigematsu, G. Yamauchi, M. Nakamura, Microstructure and mechanical properties of SUS304L stainless steel processed by equal channel angular extrusion, Journal of Materials Science Letters, 19 (2000) 2091-2093.

[26] Y. Fukuda, Processing of a low-carbon steel by equal-channel angular pressing, Acta Materialia, 50 (2002) 1359.

[27] S. Dobatkin, Bulk Nanostructured Multiphase Ferrous and Nonferrous Alloys Bulk nanostructured materials, 2009.

[28] W.J. Kim, J.K. Kim, W.Y. Choo, S.I. Hong, J.D. Lee, Large strain hardening in Ti-V carbon steel processed by equal channel angular pressing, Materials Letters, 51 (2001) 177-182.

[29] S.L. Semiatin, Workability of commercial-purity titanium and 4340 steel during equal channel angular extrusion at cold-working temperatures, Metallurgical and materials transactions. A, Physical metallurgy and materials science, 30 (1999) 1425.

[30] A. Misra, N. Li, M.S. Martin, O. Anderoglu, L. Shao, H. Wang, X. Zhang, He ion irradiation damage to Al/Nb multilayers, Journal Name: Journal of Applied Physics, (2009) Medium: ED.

[31] X. Zhang, N. Li, O. Anderoglu, H. Wang, J.G. Swadener, T. Höchbauer, A. Misra, R.G. Hoagland, Nanostructured Cu/Nb multilayers subjected to helium ion-irradiation, Nuclear Instruments and Methods in Physics Research Section B: Beam Interactions with Materials and Atoms, 261 (2007) 1129-1132.

[32] G. Ackland, Controlling Radiation Damage, Science, 327 (2010) 1587-1588.

[33] C.X. Huang, Bulk nanocrystalline stainless steel fabricated by equal channel angular pressing, Journal of materials research, 21 (2006) 1687.

[34] Formation mechanism of nanostructures in austenitic stainless steel during equal channel angular pressing, Philosophical Magazine, 87 (2007) 4949-4971.

[35] M.A. Meyers, A. Mishra, D.J. Benson, Mechanical properties of nanocrystalline materials, Progress in Materials Science, 51 (2006) 427-556.

[36] K.-T. Park, Y.-S. Kim, J.G. Lee, D.H. Shin, Thermal stability and mechanical properties of ultrafine grained low carbon steel, Materials Science and Engineering A, 293 (2000) 165-172.

VITA

Name:	Jeremy Orion Gonzalez
Address:	Department of Mechanical Engineering, Texas A&M University, 3123 TAMU, College Station, TX 77843-3123
Email Address:	csjero@gmail.com
Education:	B.S., Chemistry, Texas A&M University Kingsville, 2008 M.S., Materials Science & Engineering, Texas A&M University, 2011